

4.a Microwave Life-Detection Systems

The feasibility of the remote sensing of vital signs of human subjects using microwave radiation was demonstrated recently by us at Michigan State University [1], [2]. We will discuss two microwave life-detection systems in this chapter. The first system is an *X*-band (10 GHz) microwave life-detection system which is capable of detecting the breathing and heartbeats of a human subject lying on the ground at a distance of 30 meters or sitting behind a wall of about 6 inches thick. The second system is a *L*-band (2 GHz) microwave life-detection system which was specially designed for detecting the body movements, including the breathing and heartbeats, of human subjects located behind a very thick wall (up to a meter thick). Although these systems were originally developed for military and security purposes, they should find some medical applications, especially in the remote physiological sensing area.

The principle on which the systems can be developed is straightforward. We illuminate the subject with a low-intensity (much lower than the safety standard) microwave beam. The small amplitude body movements associated with heartbeat and breathing of the human subject will modulate the backscattered wave, producing a signal from which information of the heart and breathing rates can be extracted using phase detection in the microwave receiving system.

PHYSICAL PRINCIPLES

Some relevant physical principles involved in a physiological sensing system using microwaves are discussed here.

Doppler Effect and Phase Modulation of Microwave Signals

It is well known that when a beam of EM wave is aimed at a moving target, the reflected EM wave from the target will display a frequency shift due to the Doppler effect. The frequency shift

is given approximately by

$$\Delta f = f(v/c)$$

where Δf is the frequency shift, f is the frequency of EM wave, v is the velocity of the target relative to the EM wave source, and c is the velocity of light.

The backscattered EM wave can be expressed approximately as

$$E_s = A \cos[2\pi f(1 \pm v/c)t] \quad (4.1)$$

where the positive (negative) sign is used when the target moves toward (away from) the EM source. For example, a police radar gun using a 10 GHz microwave beam can detect a frequency shift of about 1 KHz in the reflected wave from a car traveling at a speed of 60 miles per hour. This frequency shift is sufficiently large to be measured by a conventional frequency detection system such as heterodyne system.

When an EM wave is to be used to detect a very slow movement of a target, such as the body movement associated with heartbeat and breathing, it is impractical to use the Doppler effect, because the frequency shift is extremely small due to an extremely small value of (v/c) . For this type of application, it is much more efficient to measure the phase shift in the reflected wave from the slowly moving target. Our microwave life-detection system is based on the detection of the phase modulation in the reflected wave from the human body.

When a microwave beam is incident upon a slowly moving target, the phase angle of the reflected wave will be modulated (or perturbed) by the target's movement. Mathematically, the reflected wave can be expressed as

$$E_s = A(t) \cos(2\pi ft + \Delta\phi u(t)) \quad (4.2)$$

where $\Delta\phi$ is the magnitude of the phase shift and $u(t)$ is a time function which describes the phase variation due to the target's movement. $A(t)$ is the amplitude of the reflected wave and it may also be a function of time due to the target's movement. If a microwave beam is used to detect the body movement due to heartbeat and breathing, the phase shift term ($\Delta\phi u(t)$), is very small compared with the leading term ($2\pi ft$). However, with a phase detection device, such as our microwave life-detection system, this small phase shift can be accurately measured.

A rough relation between the phase shift and the corresponding frequency shift can be given by

$$\Delta f = \frac{\Delta\phi}{2\pi} \frac{\partial u(t)}{\partial t}$$

This relation implies that for body movement due to the heartbeat of 1 Hz, the fundamental frequency shift in the reflected wave of 10 GHz is in the order of 1 Hz, because both $\partial u(t)/\partial t$ and $\Delta\phi/2\pi$ terms are in the order of unity. Obviously, it will be extremely difficult to detect a frequency shift of 1 Hz in a microwave signal of 10 GHz.

Mathematical Formulation of the Phase Modulation of a Reflected EM wave from a Moving Target

To understand how the phase angle of the reflected EM wave is perturbed by the slow movement of the human body, we will analyze the backscattered EM wave from the body when it is illuminated by a plane EM wave. To simplify the problem we model the body as a sphere of complex permittivity. The backscattered field from the sphere is well known [3]. Using the coordinate system shown in Fig.1, the expression for the backscattered electric field may be constructed as

$$\vec{E}_{bs} = \hat{x} \frac{-E_0}{2k_0 r} \sum_{n=1}^{\infty} j^n (2n+1) \left[-d_n \hat{H}_n^{(2)}(k_0 r) + j e_n \hat{H}_n^{(2)'}(k_0 r) \right] \quad (4.3)$$

where

$$d_n = \frac{\sqrt{\varepsilon_r} \hat{J}_n(k_0 a) \hat{J}_n(ka) - \hat{J}_n(k_0 a) \hat{J}_n(ka)}{\hat{H}_n^{(2)'}(k_0 a) \hat{J}_n(ka) - \sqrt{\varepsilon_r} \hat{H}_n^{(2)'}(k_0 a) \hat{J}_n(ka)} \quad (4.4)$$

$$e_n = \frac{\hat{J}_n(k_0 a) \hat{J}_n(ka) - \sqrt{\varepsilon_r} \hat{J}_n(k_0 a) \hat{J}_n(ka)}{\sqrt{\varepsilon_r} \hat{H}_n^{(2)'}(k_0 a) \hat{J}_n(ka) - \hat{H}_n^{(2)'}(k_0 a) \hat{J}_n(ka)} \quad (4.5)$$

$$\hat{J}_n(x) = \sqrt{\frac{\pi x}{2}} J_{n+1/2}(x) \quad (4.6)$$

$$\hat{H}_n^{(2)}(x) = \sqrt{\frac{\pi x}{2}} H_{n+1/2}^{(2)}(x) \quad (4.7)$$

ε_r is the complex permittivity of the sphere, a is its radius, k and k_0 represent wavenumbers inside and outside the sphere, respectively, and usual notations for Bessel functions and their derivatives are employed. E_0 is the amplitude of the incident plane wave and \hat{x} is the unit vector along the x axis.

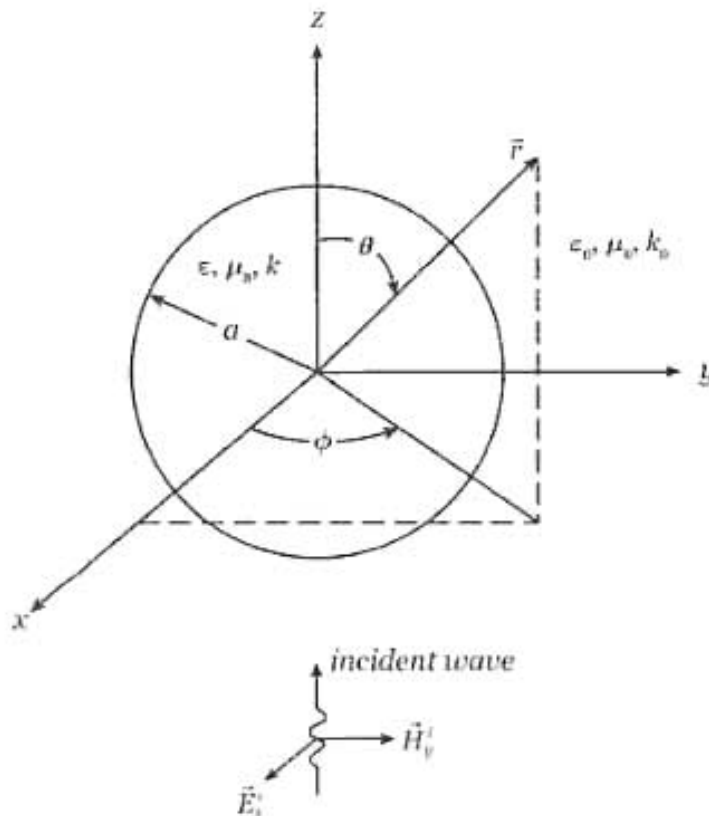


Fig. 1 A conducting sphere illuminated by an incident EM wave.

The phase and the square of the magnitude of the backscattered electric field \vec{E}_{BS} from a sphere of relative permittivity 39.9 and conductivity 10.3 S/m are depicted in Fig. 2 as functions of the radius multiplied by the wavenumber k_0 of the medium. The frequency of the microwave radiation is assumed to be 10 GHz, and the sphere is situated 30.48 m (100 ft) from the transceiver. Breathing and heartbeat produce small vibrations of the spherical surface due to changes in its radius. From Fig. 2, we conclude that these vibrations will produce a linear change in the phase and a relatively smaller linear change in the amplitude squared of the backscattered field. Similar results were obtained when the body was modeled as an infinitely long cylinder of complex permittivity, illuminated by a TM-polarized plane electromagnetic wave.

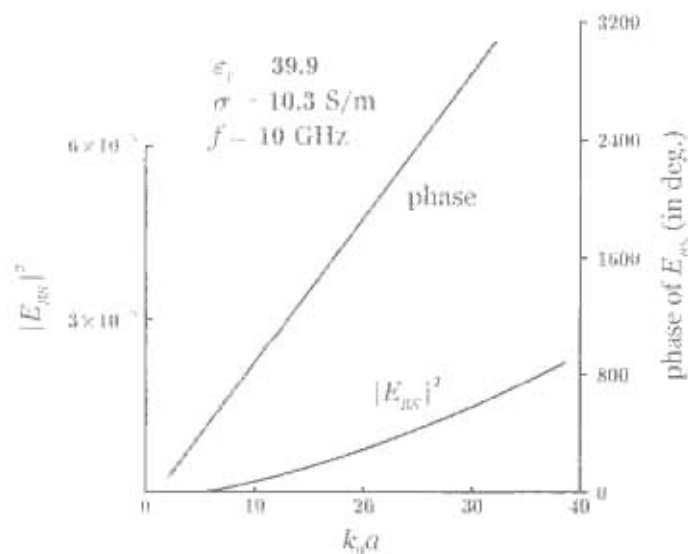


Fig. 2 Phase and magnitude squared of the backscattered field E_{BS} from a sphere as a function of $k_0 a$ at 10 GHz at a distance of 30.48 m.

These simplified models show that there will be, in general, amplitude as well as phase modulation of the incident wave as it is backscattered by the body. However, since the phase variation is more linear and it is easier to detect the phase variation from the viewpoint of the signal/noise ratio, we used the phase modulation of the backscattered wave to find the vibrations of the body surface caused by the heartbeat and breathing.

AN X-BAND MICROWAVE LIFE-DETECTION SYSTEM

In this section, the circuit diagram and operation principle of an X-band (GHz) microwave life-detection system will be described. Typical results on the measurement of heart and breathing signals will also be given.

Circuit Diagram and Operation Principle

The schematic diagram of the X-band life-detection system is shown in Fig. 3. A phase-locked oscillator at 10 GHz produces a stable output of about 20 mW. This output is amplified by a low-noise microwave amplifier to a power level of about 200 mW. The output of the amplifier is fed through a 6 dB directional coupler, a variable attenuator, a circulator, and then to a horn antenna. The 6 dB directional coupler branches out $1/4$ of the amplifier output to provide a reference signal for clutter cancellation and another reference signal for the mixer. The variable attenuator controls the power level of the microwave signal to be radiated by the antenna. Usually, the radiated power is kept at a level of about 10-20 mW. The horn antenna radiates a microwave beam of about 15° beam-width aimed at the human subjects to be monitored.

The signal received by the antenna consists of a large clutter and a weak return signal scattered from the body. To be able to detect the weak signal modulated by the body movement, the large background clutter needs to be cancelled. This is accomplished by an automatic clutter cancellation circuit which consists of a variable phase-shifter, a variable attenuator and a microprocessor unit which digitally controls the former two components. This automatic clutter cancellation circuit provides an optimal reference signal which is mixed with the received signal by the antenna in a 10 dB directional coupler for the purpose of canceling the clutter. The output of the 10 dB directional coupler contains mainly the weak scattered signal from the body. This body scattered signal is a 10 GHz CW microwave signal modulated by the breathing and the heartbeat. This signal is then amplified by a low noise microwave preamplifier (30 dB) and then mixed with another reference signal in a double-balanced mixer.

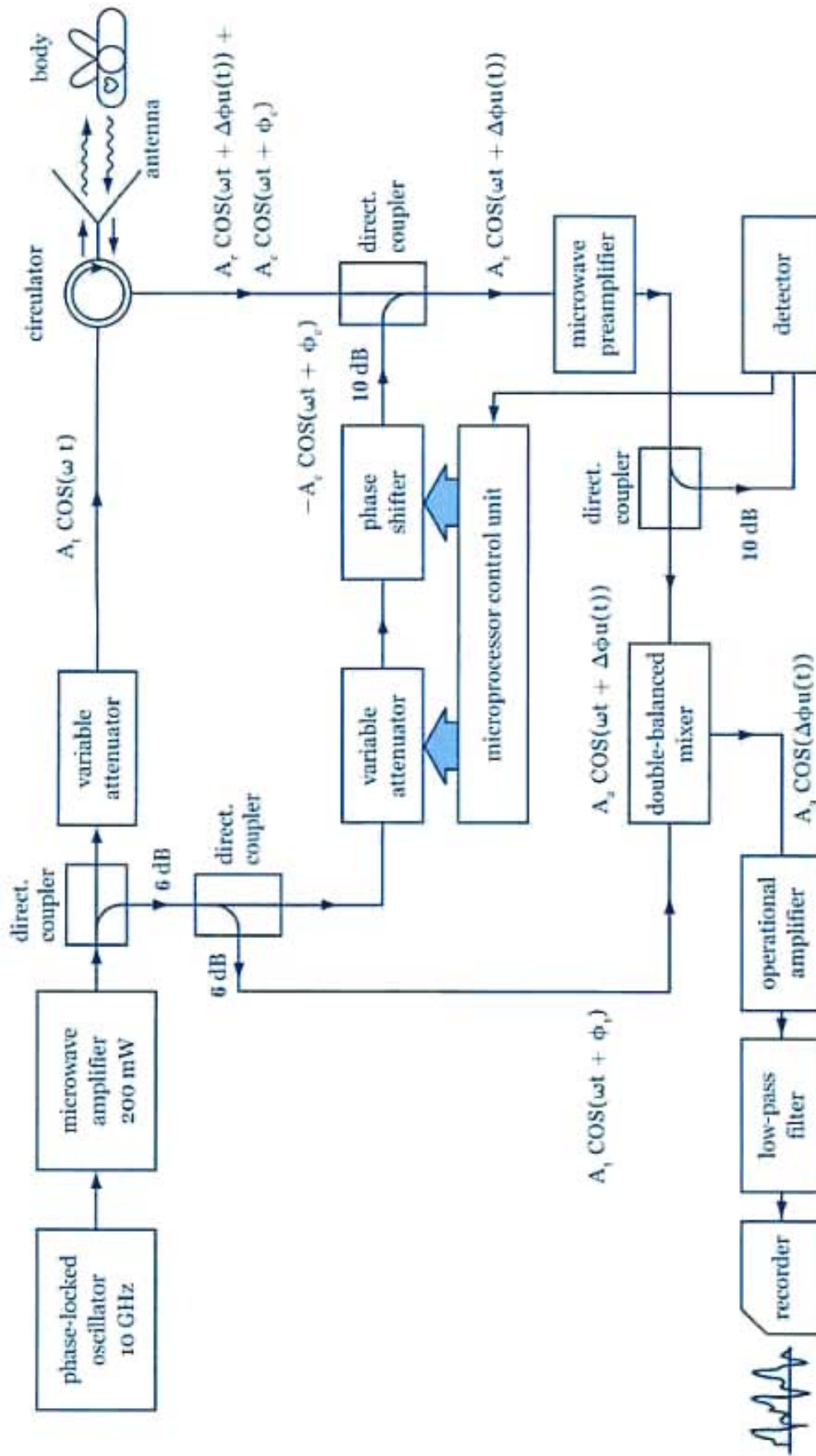


Fig. 3 Circuit diagram of the microwave life-detection system.

Reprinted from "An X-band microwave life-detection system" by Kam-Mu Chen, D. Misra, H. Wang, H. K. Chuang and E. Postou, IEEE Trans. on Biomedical Engineering, Vol. BME-33, No. 7, pp 697-701, July 1986. (C)1986 IEEE.)

Between the microwave preamplifier and the double-balanced mixer, a 10 dB directional coupler is inserted to take out a small portion of the amplifier signal for providing an input to the microprocessor unit which controls the phase-shifter and the attenuator. The optimal settings for the phase-shifter and the attenuator are determined by this input to the microprocessor unit. The mixing of the amplified, body-scattered signal and a reference signal (7-10 mW) in the double-balanced mixer produces low-frequency signals resulting from motion due to breathing and heart motion within the body. This output from the mixer is amplified by an operational amplifier and then passed through a low-pass filter (4 Hz cutoff) before reaching a recorder.

Measured Heart and Breathing Signals

Recordings of the heart and breathing signals of several persons were taken under different conditions. However, only a few of them are presented here for illustration. Fig. 4 shows the measured heart and breathing signals of a human subject lying on the ground at a distance of 30 m with a 4.5 mW, 10 GHz microwave beam aimed at him. The top graph in Fig. 4 shows the breathing signal superimposed upon the heart signal when the human subject was lying on the ground in a face-up position with the body perpendicular to the microwave beam. The middle graph in Fig. 4 shows only the heart signal when the subject was holding his breath. The bottom graph in Fig. 4 shows the background noise. The results of Fig. 4 indicate satisfactory performance of the system in detecting the heart and breathing signals of human subjects lying on the ground at a distance of 30 m or farther.

We have also studied the effect of clothing on the system performance by repeating the experiment with different clothing on the subject, e.g., up to four layers of very thick jackets. The effect of the clothing over the sensitivity of the system was found to be insignificant. Furthermore, the polarization effect of the microwave signal on the system performance was also investigated. When circular, linear-vertical, and linear-horizontal polarization were employed, the system sensitivity was found to be of the same order in all three cases.

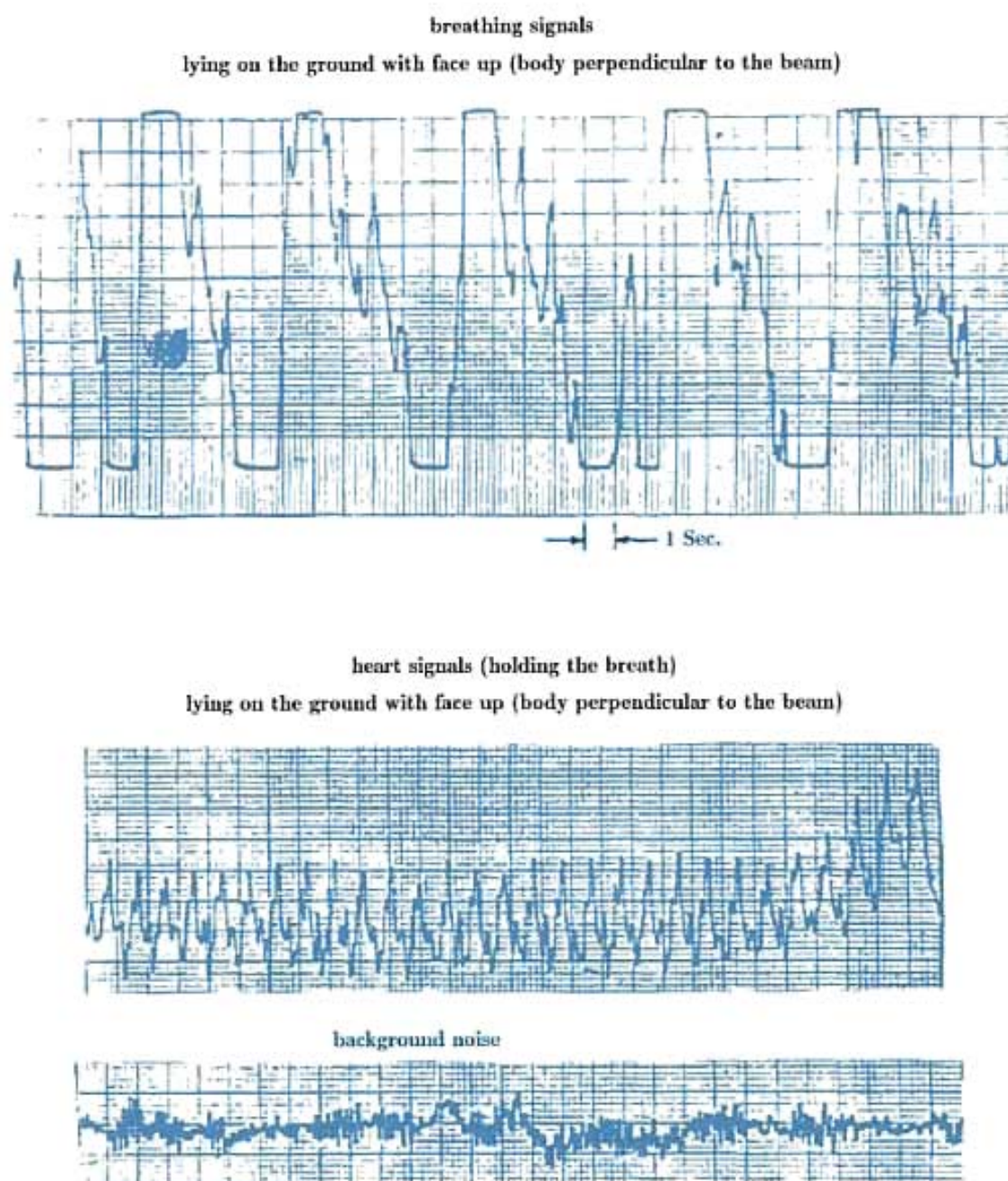


Fig. 4 Heart and breathing signals of a human subject lying on the ground at a distance of 30 m measured with a 4.5 mW, 10 GHz microwave beam.

Reprinted from "An X-band microwave life-detection system" by Kun-Mu Chen, D. Misra, H. Wang, H. R. Chuang and E. Postow, IEEE Trans. on Biomedical Engineering, Vol. BME-33, No. 7, pp 697-701, July 1986. (©1986 IEEE.)

We have also used this system to detect the heart and breathing signals of a human subject located behind a barrier with success. Fig. 5 shows the measured heart and breathing signals of a human subject sitting behind a dry 15.24 cm (6 in) cinder block wall at a distance of 0.6, 2, or 3 m. The antenna was placed close to the other side of the wall and energized to radiate 20 mW at 10 GHz. It is observed from Fig. 5 that the heart and breathing signals were clearly detected at all three distances. The background noise in each case is also shown in the figure. The results of Fig. 5 indicate that the microwave beam can penetrate the wall and a satisfactory detection of the heart and breathing signals of human subjects behind the wall is possible. We have repeated the experiment by moving both the system and the human subject away from the wall. It was found that the system could perform satisfactorily even when the human subject was 5 m away from the wall while the antenna on the other side was about 3 m from the wall. If the antenna was moved further from the wall, system performance was affected by movement of the system operator.

This life-detection system can be easily modified to produce a device for monitoring the breathing and heartbeat of a patient in a clinic. To conduct such an experiment, a metallic wire-mesh chamber with the dimensions of $2.5 \times 1 \times 0.8$ m was constructed as shown in Fig. 6. The antenna of the system was replaced by an open-ended waveguide which was mounted on a wall of the chamber. A microwave signal of $100 \mu\text{W}$ at 10 GHz was radiated into the chamber through the waveguide. A human subject was lying inside the chamber in various positions, face up, or lying on his right or left shoulder. The measured heart and breathing signals of the subject lying in these three positions are shown in Fig. 6. It is observed that a clear detection of the heart and breathing signals can be achieved. It is noted that since the microwave field is confined inside a metallic chamber and the environmental noise is minimal, only very low power microwave radiation is needed for this purpose.

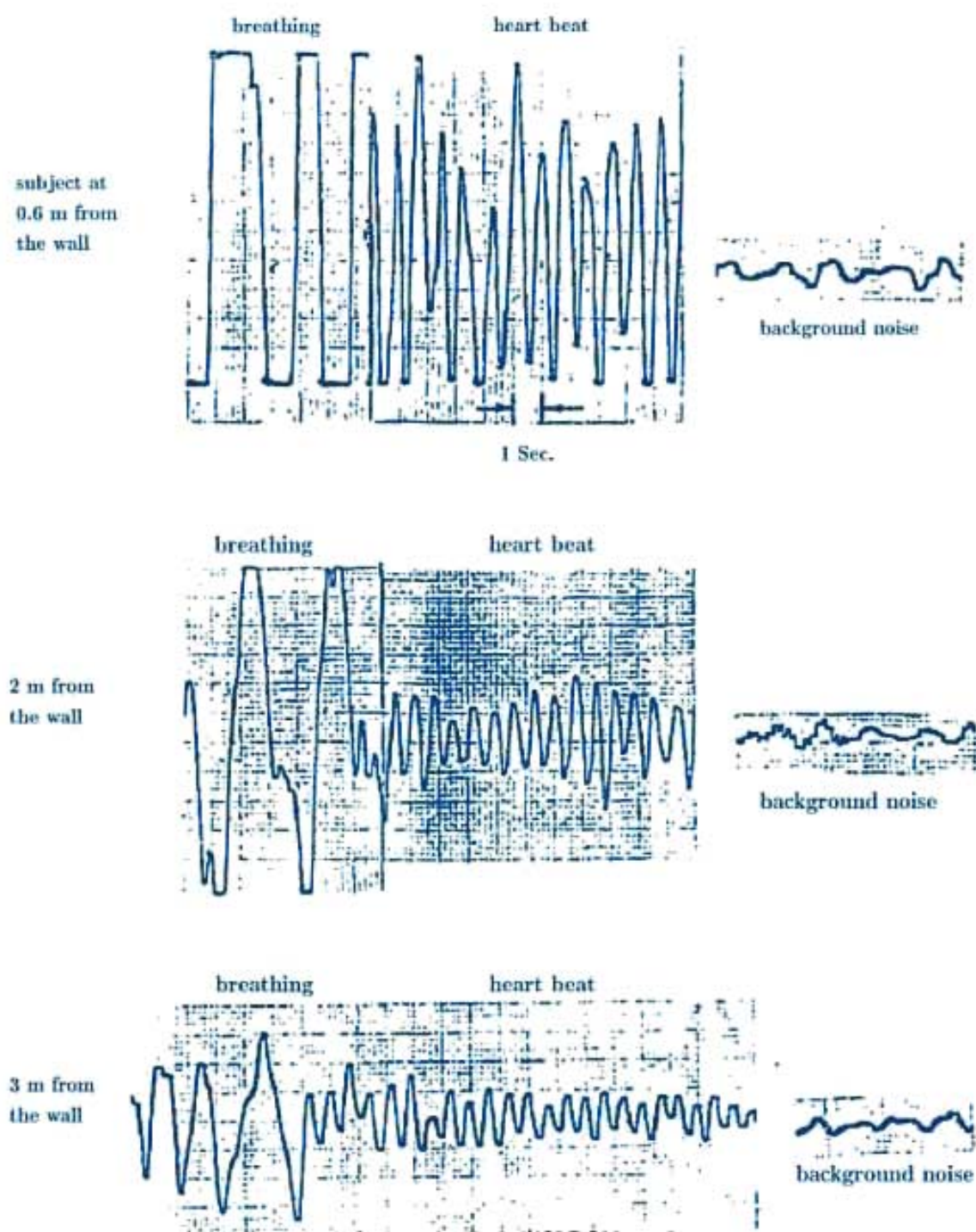


Fig. 5 Measured breathing and heart signals from a human subject sitting behind a cinder block wall (15.24 cm thick) at various distances. The antenna of the life-detection system was located on the other side of the wall and it radiated a power of about 20 mW at 10 GHz.

Reprinted from "An X-band microwave life-detection system" by Kun-Mu Chen, D. Misra, H. Wang, H. R. Chuang and E. Postow, IEEE Trans. on Biomedical Engineering, Vol. B-33, No. 7, pp 697-701, July 1986. (©1986 IEEE.)

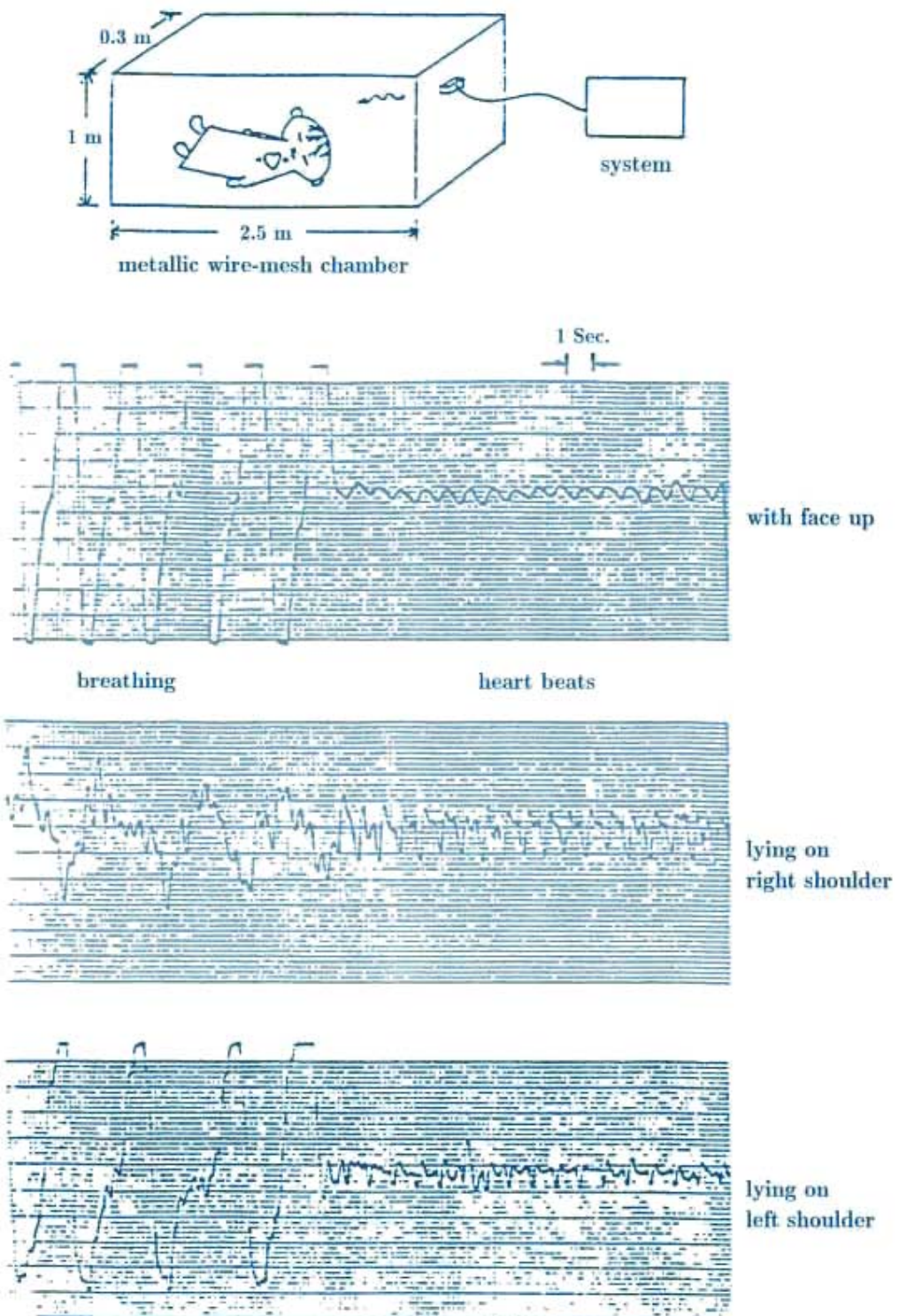


Fig. 6 Breathing and heartbeats recorded for a person lying inside a metallic wire-mesh chamber with dimensions $2.5 \times 1.0 \times 0.8$ m. The body as parallel to the radiation beam, with the head away from the antenna. Transmitted power was about $100 \mu\text{W}$.

AN L-BAND MICROWAVE LIFE-DETECTION SYSTEM

As described in the preceding section, the *X*-band microwave life-detection system can be used to detect breathing and heartbeat of a human subject located behind a brick wall of about 15 cm. However, if the wall became thicker, the detection became difficult with the *X*-band system. An *L*-band (2GHz) system was specially designed for the purpose of detecting breathing and heartbeat of a human subject who was located behind a very thick wall or buried under a thick layer of rubble.

The *L*-band system has the essentially same circuit arrangement as that of the *X*-band system, with the exception that all the components are larger because of the lower operation frequency. Since the *L*-band system operates at a much lower frequency than that of the *X*-band system, its microwave beam is more penetrating.

To test the performance of the *L*-band life-detection system, two experimental setups depicted in Fig. 7 have been used. The first setup shown in Fig. 7a consisted of a brick wall (1 m wide and 1.4 m high) of various thicknesses lined with microwave absorbers along the edge. A human subject sat behind the brick wall within a distance of 0.3 to 0.6 m. The antenna of the life-detection system was placed close to the other side of the brick wall. The second setup shown in Fig. 7b simulated a situation where a human subject was trapped under a thick layer of rubble. In this setup, various layers of bricks were laid on a wooden frame which formed a cavity for a human subject to lie down in it. Microwave absorbers were used to line the sides of this structure to prevent the microwave scattering through the sides of the brick structure. The antenna of the life-detection system was placed on the top of the brick structure aiming at the human subject under the bricks.

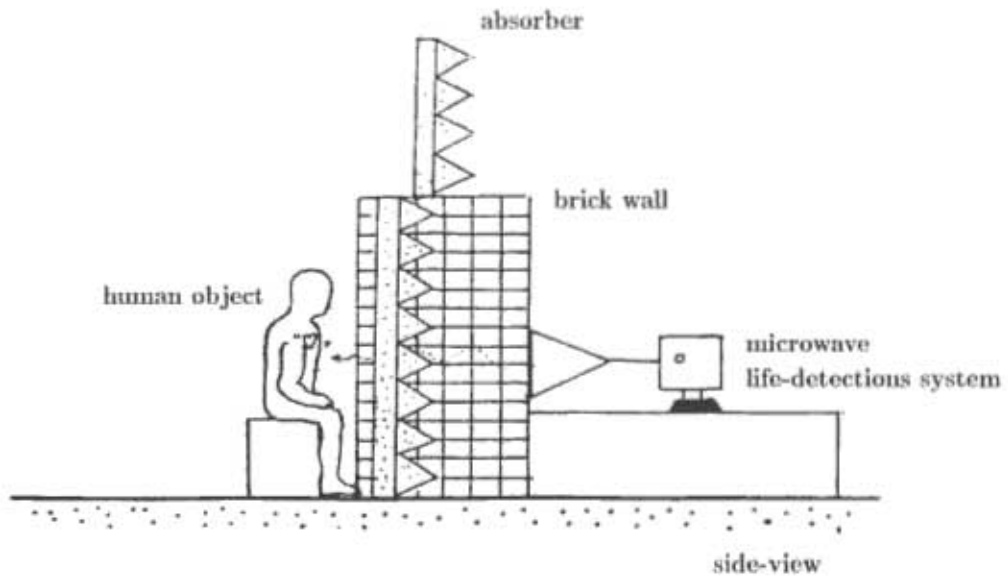


Fig. 7a

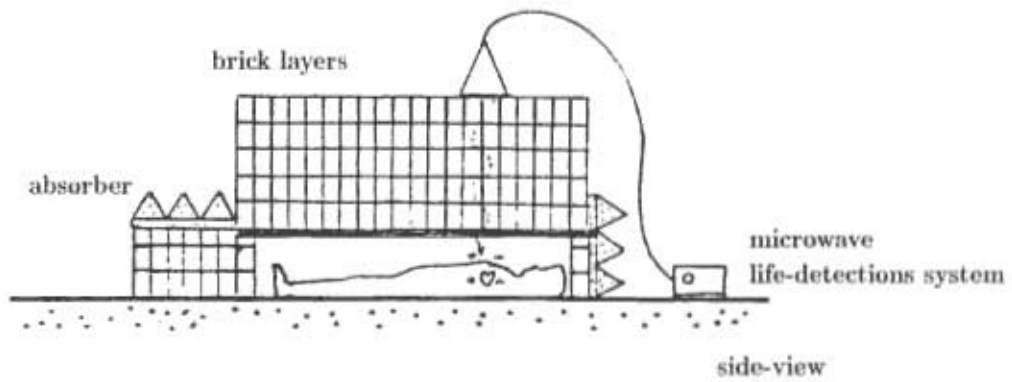


Fig. 7b

Fig. 7 Experimental setups for the measurement of heart and breathing signals of a human subject located behind or under a thick layer of bricks using the L-band (2 GHz) Microwave life-detection system.

Typical measured results on the heart and breathing signals of a human subject behind or under a thick layer of barrier are shown in Fig. 8. This figure shows the heart and breathing signals of a human subject lying with face-up or face-down position under six layers (52 cm) of dry bricks measured by the 2 GHz life-detection system. In these recorded graphs, the breathing signal, the heart signal (the subject holding his breath) and the background noise were included. It is observed that both the heart and breathing signals were clearly detected. These results demonstrate the feasibility of monitoring the physiological signs of human subjects through a thick barrier with an EM radiation with a frequency in the *L*-band or lower range.

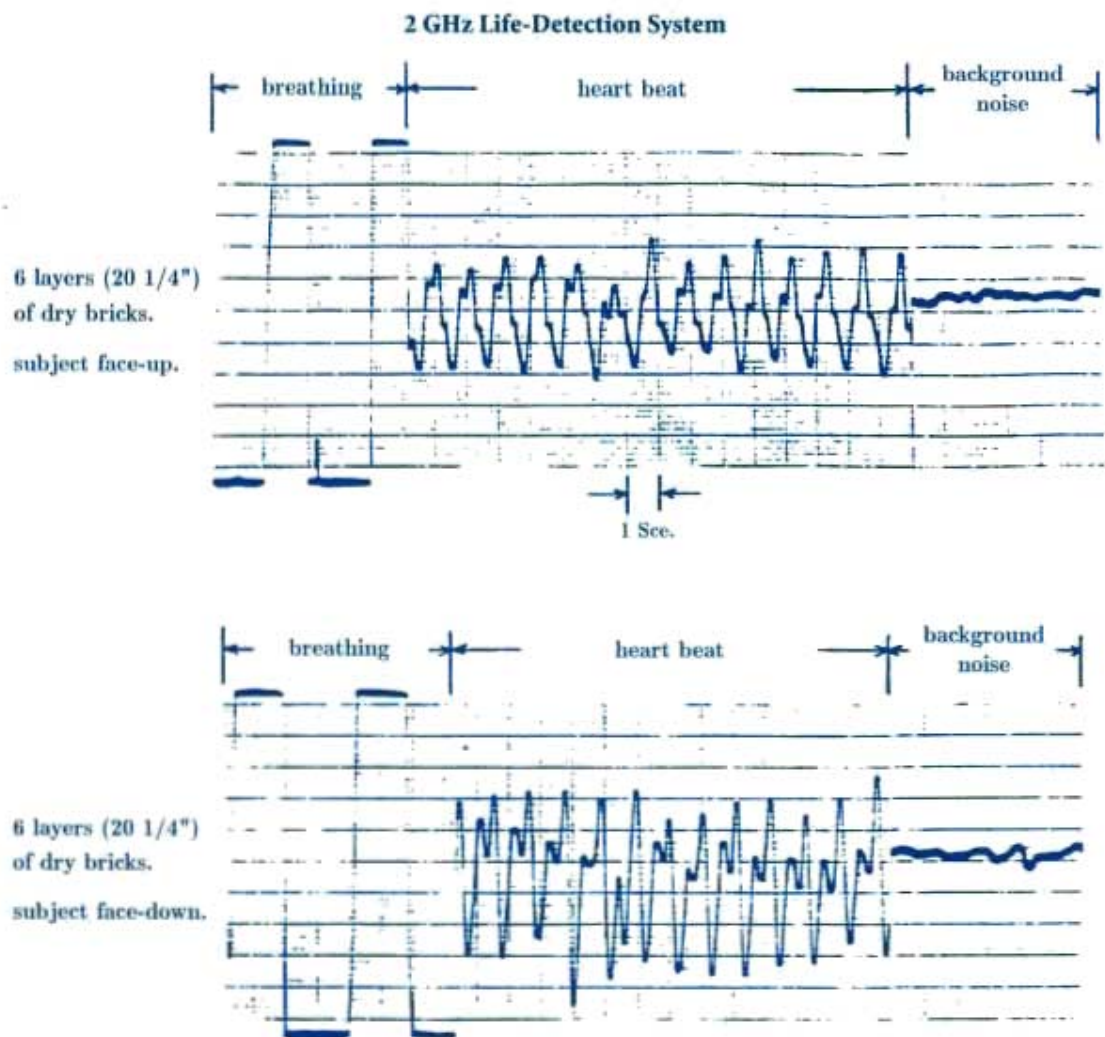


Fig. 8 Heart and breathing signals of a human subject, lying with face-up or face-down position under 6 layers of bricks, measured by the 2 GHz life-detection system.

4.b R.F. Life-Detection Systems for Searching Human Subjects Under Earthquake Rubble or Behind Barrier

In the preceding section, an *X*-band (10 GHz) and a *L*-band (2 GHz) microwave life-detection system for the remote sensing of the breathing and heartbeats of a human subject at a distance or behind a barriers were described. Those systems were found to be ineffective if a human subject is covered by a very thick layer of debris such as the earthquake rubble because a microwave radiation at *X*-band or *L*-band can not penetrate deep into debris.

Existing methods for searching and rescuing human victims buried under earthquake rubble or collapsed building debris are the utilization of dogs, or seismic or optical devices. These existing devices are not effective if the rubble or debris covering the human victims is thicker than a few feet, especially for the case when the victims are completely trapped or too weak to respond to the signal sent by the rescuers. Thus, there is great demand for constructing a new sensitive life-detection system which can be used to locate human victims trapped deep under earthquake rubble or collapsed building debris. Especially, the system needs to be sensitive enough to detect the breathing and heartbeat signals of passive victims who are completely trapped or too weak to respond to the existing seismic detection system.

A sensitive life-detection system for such purpose was constructed recently by us at Michigan Sate University [4]. This system operating at 450 MHz or at 1150 MHz will be described in this section.

The basic physical principle for the operation of a microwave life-detection system is rather simple. When an EM wave beam of appropriate frequency (*L* or *S* band) is aimed at a pile of earthquake rubble or collapsed building debris under which a human subject is buried, the EM wave beam can penetrate through the rubble or the debris to reach the subject. When the human subject is illuminated by the EM wave beam, the reflected wave from the subject will be modulated by the subject's body movements, which include the breathing and the heartbeat. If the reflected wave from the stationary background can be cancelled and the reflected wave from

the subject's body is properly demodulated, the breathing and heartbeat signals of the subject can be extracted. Thus, a human subject buried under the rubble or the debris can be located.

The system operating at 450 MHz was constructed first. This system was tested on simulated earthquake rubble constructed at the Electromagnetics Laboratory at Michigan State University, and it was also tested in a field test using realistic earthquake rubble consisted of layers of reinforced concrete slabs with imbedded metallic wire mesh at a test site in Rockville, MD, with the cooperation of the Maryland Task Force of the Federal Emergency Management Agency (FEMA). The results of these tests will be described. The second system operating at 1150 MHz was constructed after the field test at Rockville, MD. In that field test, it was found that an EM wave of 450 MHz is difficult to penetrate layers of reinforced concrete slabs with imbedded metallic wire of 4-in spacing. Through a series of experiment, we selected the operating frequency of 1150 MHz for the second system with the goal of penetrating such earthquake rubble. After the construction of the 450-MHz and the 1150-MHz systems and an extensive series of experiments, we found that an EM wave of 1150 MHz can penetrate a rubble with layers of reinforced concrete slabs with metallic wire mesh easier than that of 450 MHz. However, an EM wave of 450 MHz may penetrate deeper into a rubble without metallic wire mesh than that of 1150 MHz.

The R.F. life-detection system we constructed has four major components: 1) a microwave circuit system which generates, amplifies, and distributes microwave signals to various microwave components; 2) a microprocessor-controlled clutter-cancellation system which creates an optimal signal to cancel the clutter from the rubble and the background; 3) a dual-antenna system which consists of two separate antennas energized sequentially; and 4) a laptop computer which controls the microprocessors and acts as the monitor for the output signal. The system is operated by a portable battery unit.

Both the 450-MHz and the 1150-MHz systems are working well for various types of earthquake rubble and collapsed building debris. They can detect the breathing and heartbeat signals of trapped human subjects buried under a rubble of up to 10-ft thickness.

CIRCUIT DESCRIPTION OF THE SYSTEM

The basic circuit structures of the 450-MHz and the 1150-MHz microwave life-detection systems are quite similar and they are operated based on the same physical principle. In this section, only the circuit structure of the 1150-MHz system will be described, while that of the 450-MHz system is very similar.

The schematic diagram of the 1150-MHz microwave life-detection system is shown in Fig. 9. A phase-locked oscillator generates a very stable EM wave at 1150 MHz with an output power of 400mW (25.6 dBm). This wave is fed through a 10-dB directional coupler and a circulator before reaching a radio-frequency (RF) switch, which energized the dual antenna system sequentially. The 10-dB directional coupler branches out one-tenth of the wave (40 mW) which is then divided equally by a 3-dB directional coupler. One output of the 3-dB directional coupler (20 mW) drives the clutter cancellation circuit and the other output (20 mW) serves as a local reference signal for the double-balanced mixer.

The wave radiated by an antenna penetrates the earthquake rubble to reach a buried human subject. The reflected wave received by the same antenna consists of a large reflected wave (clutter) from the rubble and a small reflected wave from the subject's body. The large clutter from the rubble can be cancelled by a clutter canceling signal. However, the small reflected wave from the subject's body cannot be cancelled by a pure sinusoidal, canceling signal because it is modulated by the subject's motions. The dual-antenna system has two antennas, which are energized sequentially by an electronic switch. Each antenna acts independently and the final outputs from these two antennas are combined in some signal processing schemes to reduce the background noise. This part will be elaborated later.

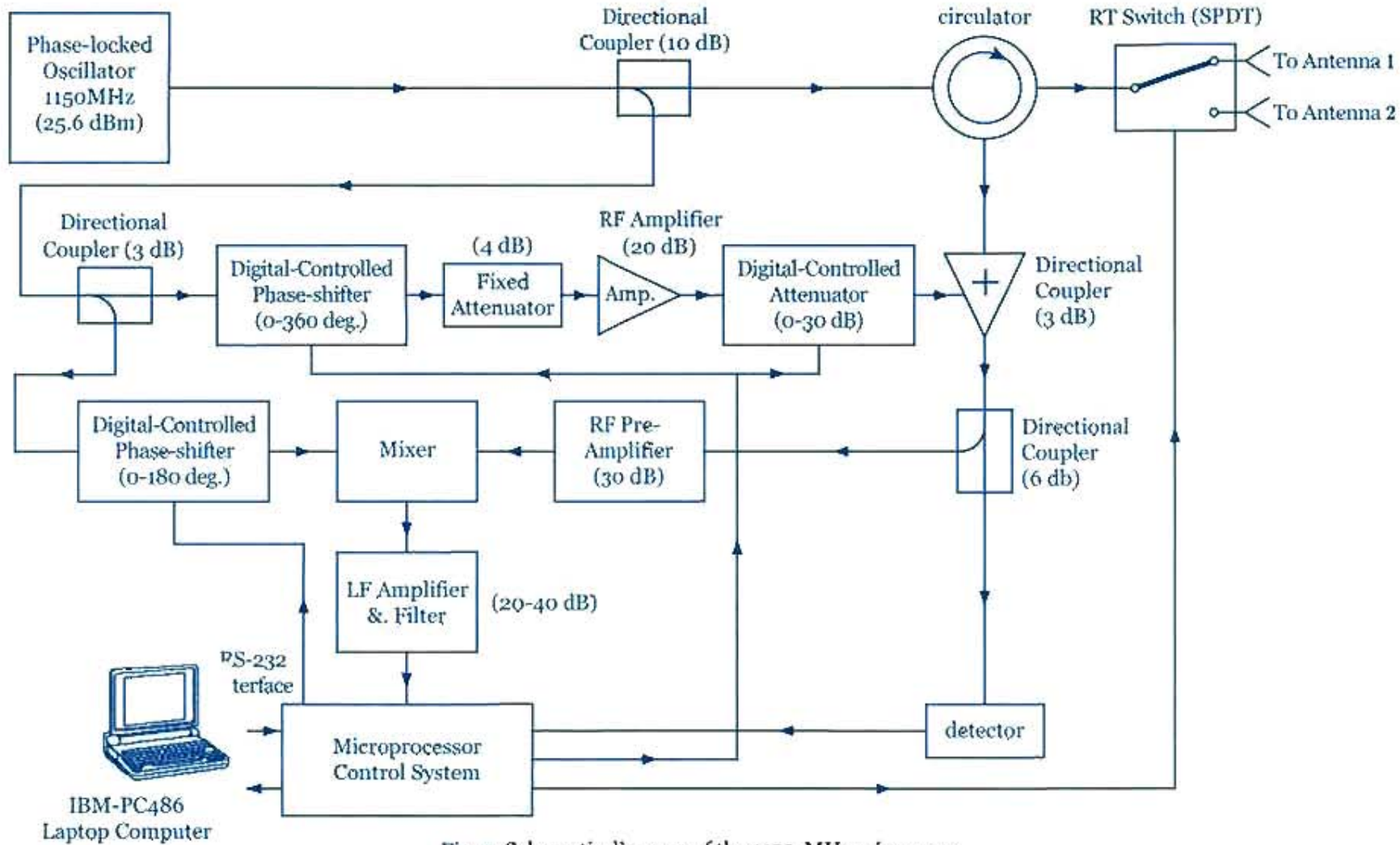


Fig. 9 Schematic diagram of the 1150-MHz microwave

Reprinted from "Microwave life detection system for searching human subjects under earthquake rubble or behind barrier" by Kun-Mu Chen, Y. Huang, J. Zhang and A. Norman, *IEEE Trans. on Biomedical Engineering*, Vol. 27, No. 1, pp. 105-114, Jan. 2000. (©2000 IEEE.)

As mentioned before, the reflected signal from the human subject after amplification by the pre-amplifier is mixed with the local reference signal in the double-balanced-mixer. The local reference signal is assumed to be $A_L \cos(\omega t + \phi_L)$ where A_L and ϕ_L are the amplitude and the phase, respectively. While the other input to the mixer, the reflected signal from the human subject, is assumed to be $A_r \cos(\omega t + \phi_E + \Delta\phi(t))$ where A_r and ϕ_E are the amplitude and the phase, respectively, and $\Delta\phi(t)$ is the phase modulation due to the body movement of the human subject. ω is the angular frequency and t is the time. When these two inputs are mixed in the double-balanced mixer, the output of the mixer will be $A_L A_r \cos(\phi_L - \phi_E - \Delta\phi(t))$.

From this expression of the mixer output, it is easy to see that

$$\text{If } \phi_L - \phi_E = (n + 1/2)\pi, \quad n = 0, 1, 2, \dots \quad (4.8)$$

the system has a maximum sensitivity;

and

$$\text{If } \phi_L - \phi_E = \pm n\pi, \quad n = 0, 1, 2, \dots \quad (4.9)$$

the system has a minimum sensitivity,

because $(\partial / \partial \Delta\phi(t)) \cos(\phi_L - \phi_E - \Delta\phi(t)) = -\sin(\phi_L - \phi_E - \Delta\phi(t))$. $\Delta\phi(t)$ is usually a small phase angle perturbation created by the body movement of the human subject. ϕ_E is the constant phase associated with the reflected signal from the human subject and it cannot be changed. ϕ_L is the phase of the local reference signal and it can be controlled by the digitally controlled phase-shifter (0° - 180°). In the operation, the phase-shifter will automatically shift in such a way that $\phi_L - \phi_E$ is nearly $(n+1/2)\pi$ to attain a maximum system sensitivity.

ANTENNA SYSTEM

We have designed and constructed three types of antennas for the microwave life-detection system. They are: 1) the reflector antenna; 2) the patch antenna; and 3) the probe antenna. Each antenna simultaneously acts as the radiating element and the receiving element. It radiates EM wave through the earthquake rubble to reach the trapped human subjects and at the same time it receives the reflected EM wave from the rubble and the human subjects. The antenna can perform two functions simultaneously with the help of a circulator, which separates the radiating EM wave from the received EM wave.

The reflector antenna was constructed with two aluminum plates as the reflectors and an adjustable dipole antenna as the driving element. The two aluminum plates with the dimensions of 21 in \times 11 in form a corner reflector with the dipole antenna as its primary radiator. The angle between the two aluminum plates is adjustable and they are folded together when it is not used. The dipole antenna is a conventional, half-wavelength electric dipole. The reflector antenna is a simple, lightweight, and rugged structure and it performs very well in the most of situations.

The gain of the reflector antenna is difficult to define and measure because the antenna is placed directly over a rubble pile and the scattered field of the antenna is strongly dependent on the nature of the rubble material.

A patch antenna was constructed for radiating and receiving EM wave for the microwave life-detection system. The patch antenna consists of an aluminum ground plane, which is supported by four legs and a strip plate of about a half-wavelength, which is attached to the ground plane and fed by a coaxial line. The strip plate is insulated from the ground plane. The coaxial cable is attached to the ground plane through a connector.

The performance of the patch antenna is not better than that of the reflector antenna. It only serves as alternative type of antenna and may be useful in some situations.

A probe antenna was designed to insert through boreholes or naturally occurring fissures into the earthquake rubble to seek for the trapped victims. Physically, a probe antenna should

have a cylindrical wire structure and its radius be kept as small as possible. We have designed a probe antenna, which is essentially a sleeve antenna, as shown in Fig. 10.

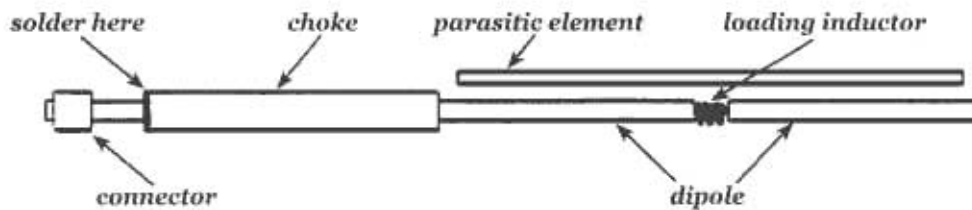


Fig. 10 Probe antenna for the life-detection system.

The radiating element is a half-wavelength dipole, which is loaded with an inductor at the center. The inductance of the inductor was determined numerically in the design. One half of the dipole is connected to the center conductor of the coaxial cable via the inductor. The other half of the dipole is a quarter-wavelength section of the outer surface of the coaxial cable. A quarter-wavelength choke, which is cylindrical tubing of larger radius than that of the coaxial cable, is soldered to the coaxial cable at one end and kept open at the other end. This choke is acting as a shorted, quarter-wavelength transmission line, which provides very high input impedance at the end point of the radiating dipole. Thus, this choke will stop the unbalanced current leaking to the outer surface of the connecting cable. A parasitic element, a wire of slightly shorter than half-wavelength, is placed next to the radiating dipole to increase the bandwidth of the antenna. The selection of dimensions of the parasitic element was made empirically through an experiment with a network analyzer. The whole structure of the probe antenna is encased in a rugged plastic tubing.

The dual antenna system has two antennas, which are energized sequentially by an electronically controlled microwave single-pole double-throw (SPDT) switch. The SPDT switch turns on and off at a frequency of 100 Hz which is much higher than the frequency range of the breathing and heartbeat signals between 0.2 Hz and 3 Hz. Thus, we can consider that the two antennas essentially sample their respective objects at the same time. In this dual-antenna system, the two antenna channels are completely independent.

EXPERIMENTAL RESULTS

The 450- and 1150-MHz microwave life-detection systems were tested in a simulated earthquake rubble constructed at the Electromagnetics Laboratory of Michigan State University. The 450-MHz system was also tested in a field-test with realistic rubble conducted at Montgomery County, Rockville, MD, with the cooperation of Maryland Task Force of FEMA. Typical experimental results of these systems are summarized here.

A. Experimental Results Obtained with the 450-MHz System at a Simulated Rubble in MSU Laboratory

The 450-MHz microwave life-detection system was tested in simulated rubble constructed in the Electromagnetics Laboratory of Michigan State University. The rubble is depicted in Fig. 11. It was constructed with bricks, cinder blocks, and steel re-bars. The dimensions of the rubble was about 5 ft wide, 6 ft long, and 6 ft high. Two layers of steel re-bars separated by 8 in are placed perpendicularly through bricks as shown in Fig. 11. A human subject to be tested can lie down in the cavity at the bottom of the rubble. A reflector antenna or a patch antenna can be placed on the top of the rubble, while a probe antenna can penetrate into the rubble through a hole in the rubble.

Typical experimental results of the breathing and heartbeat signals of a human subject lying in the rubble cavity obtained with the 450-MHz system are shown in Figs. 12 and 13.

Fig. 12 shows a breathing signal superimposed with a heartbeat signal recorded for a female human subject. A reflector antenna was used and the radiated power was about 300 mW. The upper graph is the time domain measured signal and the lower graph is the fast Fourier transform (FFT) of the time-domain signal, which shows the frequency components of the time-domain signal. The upper graph clearly shows the breathing and heartbeat signals. The frequency domain FFT results show that the time-domain signal has a breathing signal of 0.3 Hz (the dominant

peak) and a heartbeat signal of 1.36 Hz (the second largest peak). The other peak at 0.6 Hz (the third largest peak) is the second harmonic of the breathing signal. Other small peaks are due to noise or harmonics of the breathing and heartbeat signals. From a signal as shown in Fig. 12, it is easy to identify the breathing and heartbeat signals from either the time-domain signal or the frequency domain FFT results, and a buried human subject is easily detected.

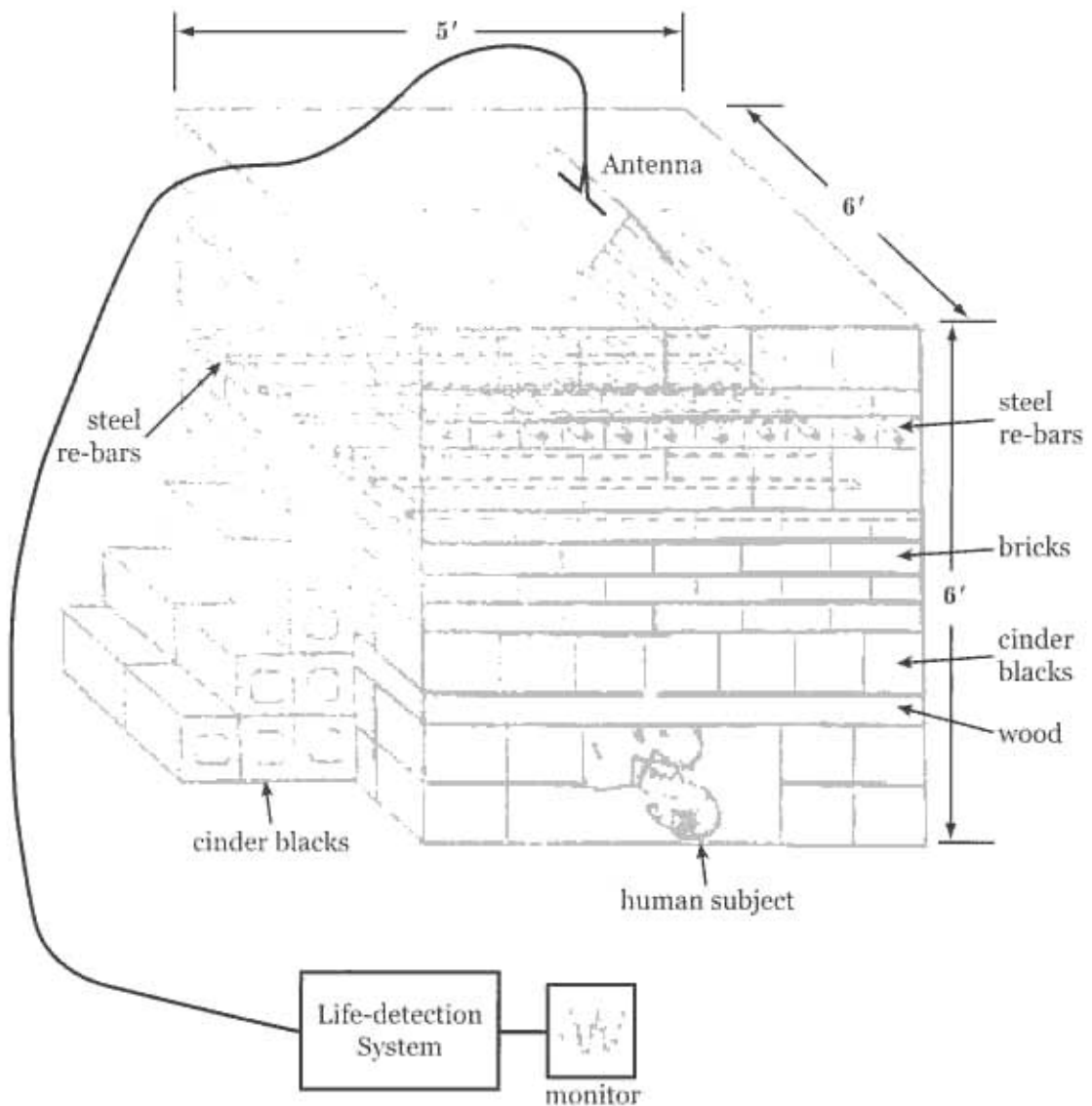


Fig. 11 Simulated earthquake rubble constructed at the Electromagnetics Laboratory of Michigan State University.

Reprinted from "Microwave life detection system for searching human subjects under earthquake rubble or behind barrier" by Kun-Mu Chen, Y. Huang, J. Zhang and A. Norman, *IEEE Trans. on Biomedical Engineering*, Vol. 27, No. 1, pp. 105-114, Jan. 2000. (©2000 IEEE.)

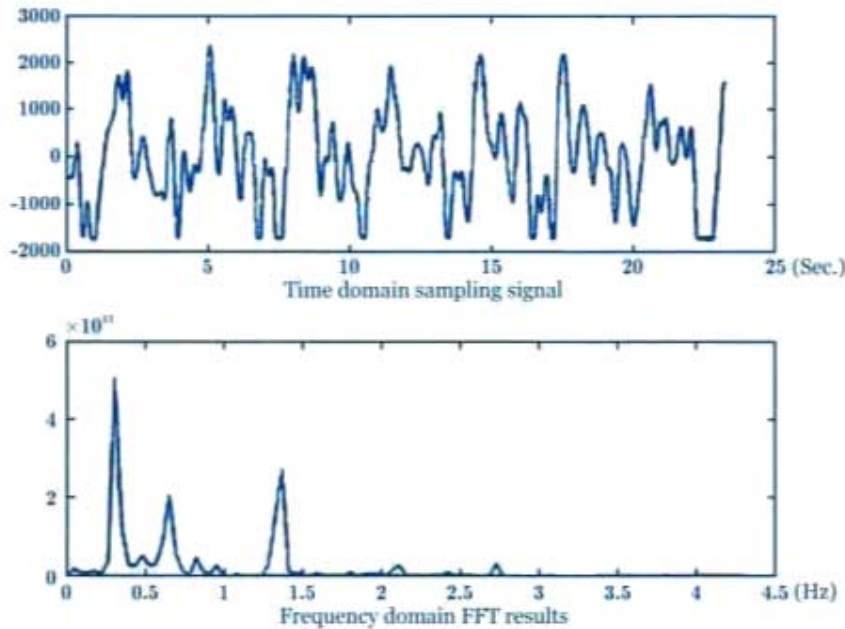


Fig. 12 Breathing and heartbeat signals of a female human subject recorded at MSU simulated rubble. A reflector antenna was placed on the top of the rubble and the female human subject was lying inside the rubble cavity. The radiated power is about 300 mW. The 450-MHz life-detection system was used.

Reprinted from "Microwave life detection system for searching human subjects under earthquake rubble or behind barrier" by Kun-Mu Chen, Y. Huang, J. Zhang and A. Norman, IEEE Trans. on Biomedical Engineering, Vol. 27, No. 1, pp. 105-114, Jan. 2000. (©2000 IEEE.)

Fig. 13 shows the same measurement conducted on the same subject when she was holding her breath. The time-domain signal (upper graph) shows only the heartbeat signal and the frequency domain FFT results (lower graph) shows only a single dominant peak of heartbeat signal at 1.36 Hz. Other small peaks are probably due to noise. It is noted that when the signals of Figs. 12 and 13 are compared, the amplitude of heartbeat signal is found to be significantly smaller than that of the breathing signal as expected.

Fig. 14 shows the background noise recorded when no human subject was in the rubble cavity. It is noted that the amplitude of the noise is lower than that of the breathing signal and the noise has wide spread frequency components as indicated in its FFT results. It is easy to distinguish the noise from the breathing and heartbeat signals from the amplitude and the frequency contents of the recorded signals.

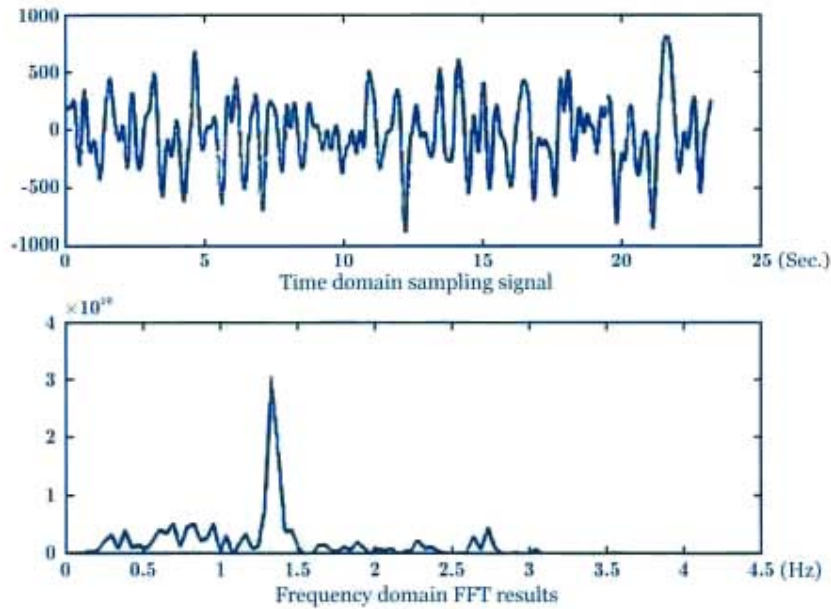


Fig. 13 Heartbeat signal of a female human subject recorded at MSU simulated rubble. A reflector antenna was placed at the top of the rubble and the female human subject lying inside the rubble cavity was holding her breath. The 450-MHz life-detection system was used.

Reprinted from "Microwave life detection system for searching human subjects under earthquake rubble or behind barrier" by Kun-Mu Chen, Y. Huang, J. Zhang and A. Norman, IEEE Trans. on Biomedical Engineering, Vol. 27, No. 1, pp. 105-114, Jan. 2000. (©2000 IEEE.)

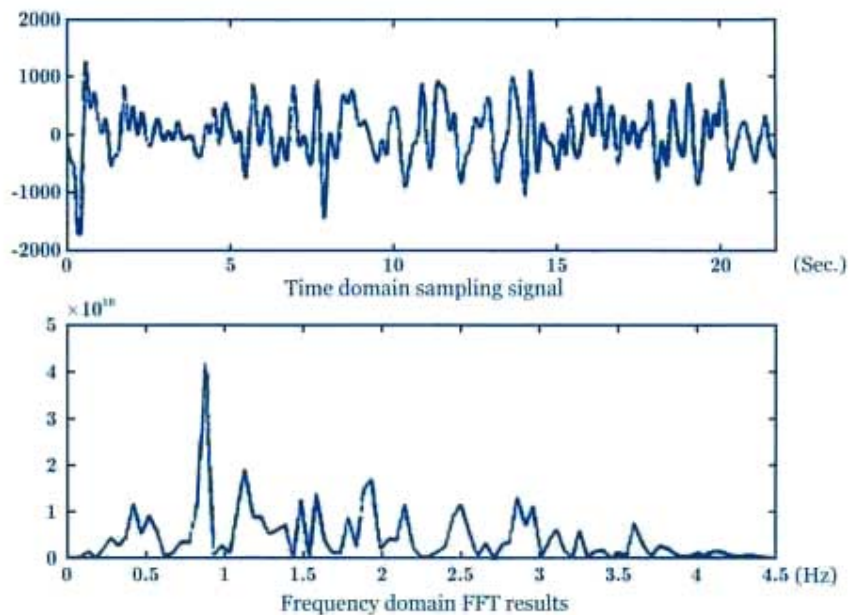


Fig. 14 Background noise recorded at MSU simulated rubble when no human subject was inside the rubble cavity. The 450-MHz life-detection system was used.

Reprinted from "Microwave life detection system for searching human subjects under earthquake rubble or behind barrier" by Kun-Mu Chen, Y. Huang, J. Zhang and A. Norman, IEEE Trans. on Biomedical Engineering, Vol. 27, No. 1, pp. 105-114, Jan. 2000. (©2000 IEEE.)

B. Experimental Results Obtained with the 450-MHz System in the Field Test Conducted at Rockville, MD

On July 5–7, 1995, a field test managed by Maryland FEMA Task Force was conducted at its Montgomery County training ground. They constructed three rubble structures using reinforced concrete slabs and double-T structures for the test. The first rubble having a height of 6 ft was constructed with seven layers of reinforced concrete slabs placed on the top of a double-T structure, simulating a collapsed seven-story building. The second rubble having a height of 9 ft was constructed with six layers of reinforced concrete slabs on the top of two double-T structures. The third rubble was constructed with pieces of reinforced concrete blocks piled on the top of a reinforced concrete pipe, which had a diameter of about 2 ft, and a fine metallic wire mesh imbedded. Also there was wet soil mixed in the rubble and the rubble was directly under large trees. The height of this rubble was about 9 ft. This rubble used in the field test is much more difficult for an EM wave of 450 MHz to penetrate than the simulated rubble used in MSU Laboratory because of the dimensions and the contents of the rubble and many layers of metallic wire mesh present in the rubble.

Many experimental results were recorded for various conditions by changing the locations of antenna and human subjects and using different rubble. However, only some of the test results measured at the second rubble, as depicted in Fig. 15, will be presented here for brevity.

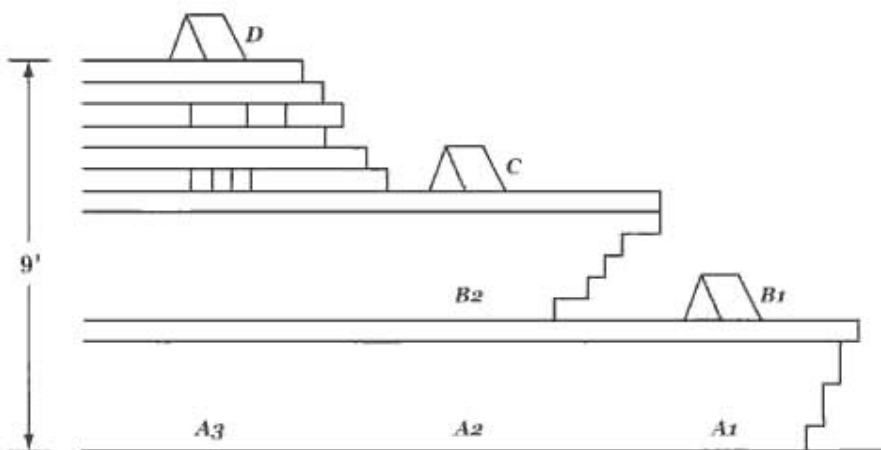


Fig. 15 The second earthquake rubble constructed at Montgomery County, Rockville, MD.

Fig. 16 shows the results of a test conducted at the second rubble, with the reflector antenna placed at location *B1* and a human subject lying at location *A1*. In this case, the EM wave needed to penetrate only one double-T structure, therefore a very strong breathing signal was recorded. The time-domain signal showing a strong breathing signal was recorded. The time-domain signal shows a strong breathing signal (over the scale) and its FFT results show a single dominant peak at 0.26 Hz. Because of the overwhelmed breathing signal the heartbeat signal was overshadowed.

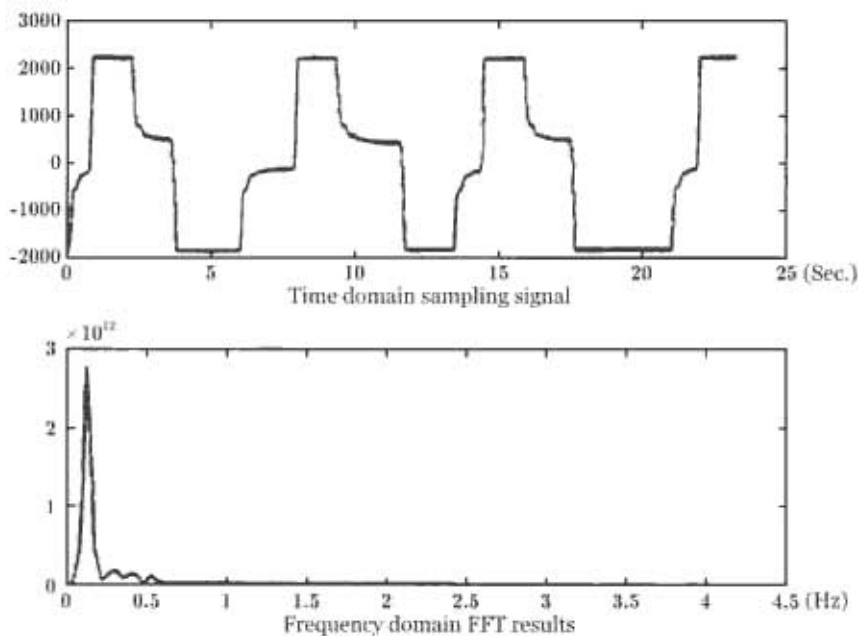


Fig. 16 Breathing signal of a human recorded at the second rubble, with a reflector antenna at location *B1* and the human subject lying at location *A1*. The 450-MHz life-detection system was used.

Reprinted from "Microwave life detection system for searching human subjects under earthquake rubble or behind barrier" by Kun-Mu Chen, Y. Huang, J. Zhang and A. Norman, IEEE Trans. on Biomedical Engineering, Vol. 27, No. 1, pp. 105-114, Jan. 2000. (©2000 IEEE.)

Fig. 17 presents the results of a test conducted at the second rubble, with the reflector antenna placed at location *D* and a human subject lying near location *A3*. In this case, the EM wave needed to penetrate six layers of reinforced concrete slabs and two double-T structures. Because of a great depth (about 9 ft) of dense rubble existed between the antenna and the human subject, the magnitude of the received signal was considerably reduced. The time-domain signal shows a distinctive breathing signal and a mixture of heartbeat signal and noise. However, its FFT results clearly identify the breathing signal and a possible heartbeat signal. It is noted that two peaks appeared near 0.2–0.3 Hz may be due to the uneven breathing pattern of the human subject under test.

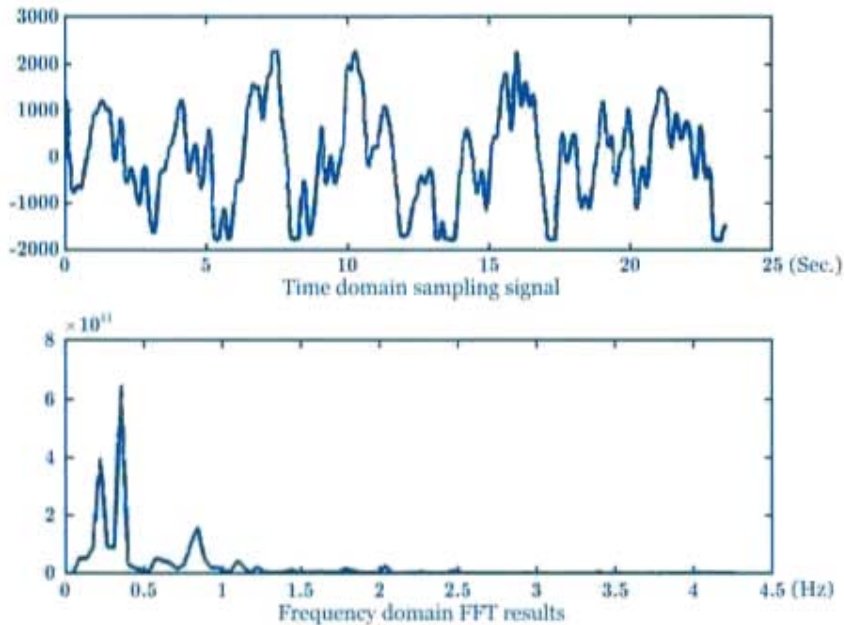


Fig. 17 Breathing and heartbeat signals of a human subject recorded at the second rubble, with a reflector antenna placed at location *D* and the human subject lying near location *A3*. The 450-MHz life-detection system was used.

Reprinted from "Microsecond life detection system for searching human subjects under earthquake rubble or behind barrier" by Kun-Mu Chen, Y. Huang, J. Zhang and A. Norman, IEEE Trans. on Biomedical Engineering, Vol. 27, No. 1, pp. 105-114, Jan. 2000. (©2000 IEEE.)

Fig. 18 shows the measured background noise when no human subject was present under the rubble pile. It is noted that the amplitude of the time-domain signal was reduced one order of magnitude from the case when a human subject was present under the rubble pile. The FFT results showed the presence of wide spread frequency components implying a random noise. However, it is pointed out that the two large peaks near 0.3 and 1.3 Hz were also recorded. It is suspected to be contributed by the operator taking the measurement. This may cause misjudgment in the rescue effort. To avoid this problem, when the measured signal is very low and peaks indicating potential breathing or heartbeat signals are present, the operator needs to move around to check his potential interference. This problem can also be mitigated by a dual-antenna system as discussed later.

The performance of the 450-MHz system at the field test was satisfactory. However, it was also found that an EM wave of 450 MHz does not penetrate well a rubble consisting of layers of reinforced concrete slabs with imbedded metallic wire mesh of 4-in spacing. To overcome this

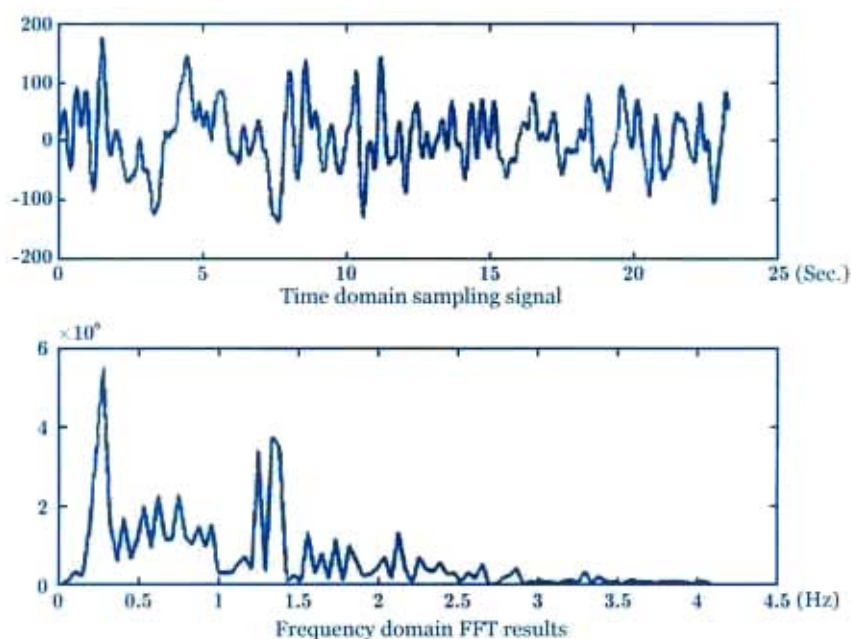


Fig. 18 Background noise recorded when no human subject was inside the rubble. The 450-MHz life-detection system was used.

Reprinted from "Microwave life detection system for searching human subjects under earthquake rubble or behind barrier" by Kun-Mu Chen, Y. Huang, J. Zhang and A. Norman. IEEE Trans. on Biomedical Engineering, Vol. 27, No. 1, pp. 105-114, Jan. 2000. (©2000 IEEE.)

by the artificial heart because the artificial breather was shut off. The thrust of these three figures is to show that the detection of the heartbeat signal can be enhanced if the two sets of signals received by antenna *A* and antenna *B* are crosscorrelated.

Fig. 19 shows the heartbeat signals created by the artificial heart and measured by reflector antenna *A* and reflector antenna *B* which were placed 7 ft directly above the target. The time-domain results of both antennas show the heartbeat signals contaminated by a large noise. Their FFT results also show the presence of a strong noise with spread frequencies. However, when these two sets of signals were crosscorrelated, a distinctive peak of the heartbeat signal at 0.8

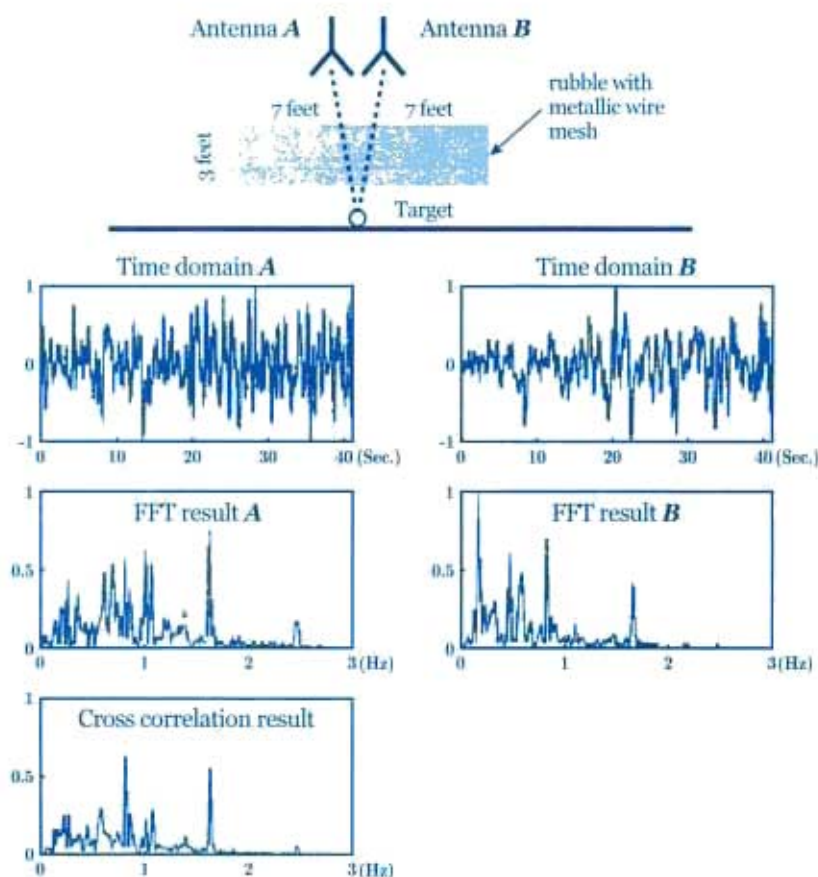


Fig. 19 Heartbeat signals measured by two-reflector antennas arranged symmetrically. Both time-domain and FFT results are shown. The cross-correlation result of the two sets of results shows two peaks representing the heartbeat frequency and its second harmonic. The 1150-MHz life-detection system was used.

Reprinted from "Microwave life detection system for searching human subjects under earthquake rubble or behind barrier" by Kun-Mu Chen, Y. Huang, J. Zhang and A. Norman, IEEE Trans. on Bio-medical Engineering, Vol. 27, No. 1, pp. 105-114, Jan. 2000. (©2000 IEEE.)

Hz appeared. A second distinctive peak at 1.6 Hz is the second harmonic of the heartbeat signal. It is also observed that the noise measured by both antennas was drastically reduced. From this cross-correlated result, the heartbeat signal was clearly detected.

Fig. 20 shows the heartbeat signals measured by two different types of antennas. The reflector antenna *A* was placed 7 ft above the target and the probe antenna *B* was inserted through the rubble to reach a point 3.5 ft from the target. The time-domain signals measured by both antennas are shown. For this case the FFT results of these two sets of signals both show a distinctive heartbeat signal and its harmonics. When these two sets of signals are crosscorrelated, a more distinctive heartbeat signal at 0.8 Hz and its second harmonic at 1.6 Hz are produced.

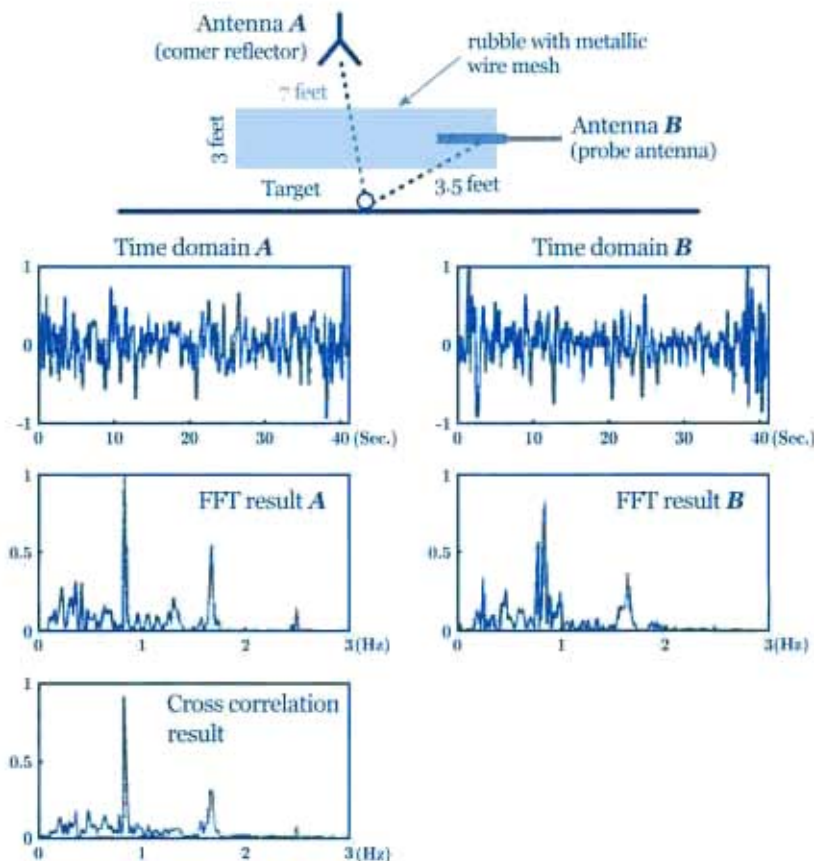


Fig. 20 Heartbeat signals measured by a reflector antenna and a probe antenna. Both time-domain and FFT results are shown. The cross-correlation result of the two sets of results shows the heartbeat frequency and its second harmonic. The 1150-MHz life-detection system was used.

Reprinted from "Microwave life detection system for searching human subjects under earthquake rubble or behind barrier" by Kun-Mu Chen, Y. Huang, J. Zhang and A. Norman, IEEE Trans. on Biomedical Engineering, Vol. 27, No. 1, pp. 105-114, Jan. 2000. (©2000 IEEE.)

Fig. 21 shows the heartbeat signals measured by reflector antenna A and reflector antenna B both placed 7 ft above the target when a human operator was walking near the rubble, about 20 ft from the antenna. The walking human subject created a large interference signal in the outputs of antenna A and antenna B showing both in their time-domain results and the FFT results. When those two sets of signals were crosscorrelated, the heartbeat signal of 0.8 Hz and its second harmonic of 1.6 Hz appeared while the interference signal nearly disappeared. From this result, we can conclude that the dual-antenna system of the 1150-MHz can be used to reduce the interference noise created by the system operators moving near the rubble as well as the background noise.

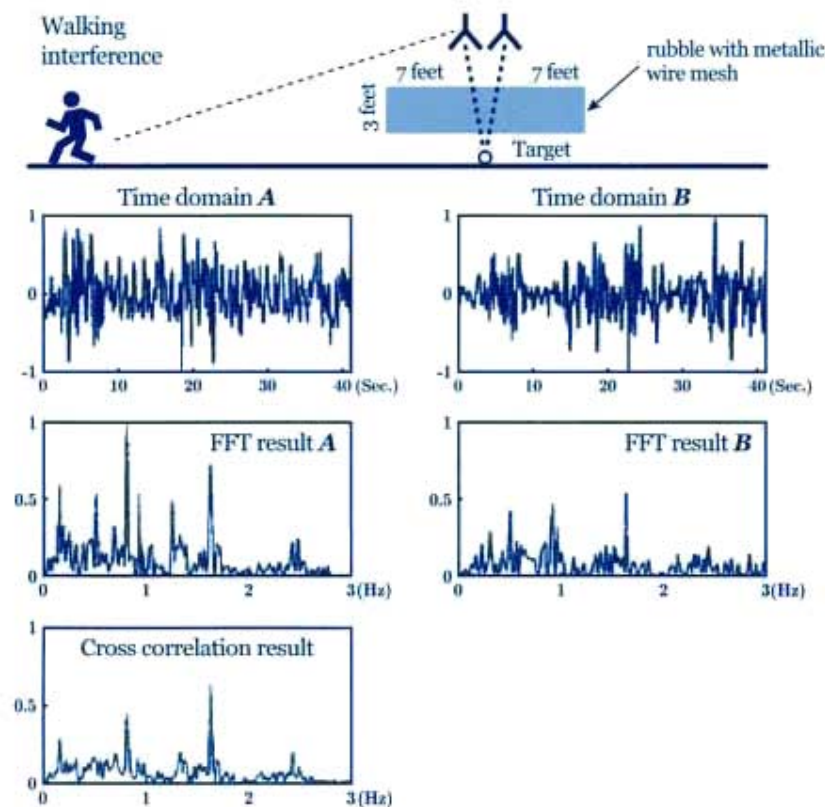


Fig. 21 Heartbeat signals measured by two reflector antennas while a human operator was walking near the rubble. Both time-domain and FFT results are shown. The cross-correlation result of the two sets of results shows the heartbeat frequency and its harmonic, while the interference signal created by the operator nearly disappears. The 1150-MHz life-detection system was used.

Reprinted from "Microwave life detection system for searching human subjects under earthquake rubble or behind barrier" by Kun-Mu Chen, Y. Huang, J. Zhang and A. Norman, *IEEE Trans. on Biomedical Engineering*, Vol. 27, No. 1, pp. 105-114, Jan. 2000. (©2000 IEEE.)

4.c Analysis of Interaction Between ELF-LF Electric Fields and Human Bodies*

The interaction of extremely low frequency (ELF, 0-100 Hz) electromagnetic (EM) fields with the human body has become an increasingly important subject since potential health hazards due to the EM fields emitted by extremely high-voltage (EHV) power lines and ELF antenna systems became a public concern.

This subject has been extensively investigated experimentally or empirically by many workers [5]-[10]. However, all of the experiments were conducted on animals or scale models of man, and it is necessary to extrapolate these experimental data to provide data for human risk analysis. This is not an easy task if a reliable theoretical method for predicting the interaction of ELF fields with the human body is not available.

Theoretical studies on this subject have been conducted by a number of researchers, but they invariably used oversimplified body geometries or inaccurate methods. Shiau and Valentino [11] have used spheroidal models of man and their results from this idealized model may have little practical value. Spiegel [12], [13] used a more accurate block model and an electric field integral equation method, but his results disagree with experimental results mainly due to insufficient partition of the body model in the numerical calculation. Chiba et al. [14] used a finite-element method and a body of revolution geometry. Their results are still not accurate for a realistic human body. Kaune and McCreary [15] developed a numerical method on a cylindrical model of man. Since this model is over-simplified, the practical values of their results are questionable.

We have developed a numerical method which utilizes a realistic model of man with arbitrary shape and posture, and a realistic environmental condition such as assuming arbitrary grounding impedances between some parts of the body and ground [16]. Our method is developed on the basis of an integral equation for the induced surface-charge density, Ohm's law, and the

*The material in this section is based on "Quantification of interaction between ELF-LF electric fields and human bodies" by Kun-Mu Chen, Heuy-Ru Chuang and Chun-Ju Lin, which appeared in *IEEE Transactions on Biomedical Engineering*, Vol. BME 33, No. 8, pp. 746-756, Aug. 1986 (©1986 IEEE.)

conservation of electric charge. The accuracy of our method has been checked with the exact solutions of a spherical and a spheroidal body. In addition, it has been verified by experimental results [9], [10] on the induced electric fields at the surface of the body, the short-circuit current, and the induced current density inside the body at 60 Hz. We have also found that it was possible to predict environmental results on the interaction of the human body with HF fields [17] with our method. This seems to extend the validity of our method to LF or even up to the HF range. It is also noted that our method is numerically quite efficient.

We will describe the theoretical development of our numerical method and reports some results on the induced electric fields at the body surface and inside the body, the induced current density inside the body, the short-circuit current, and the effects of the grounding impedance on the induced current in a homogeneous body of realistic shape.

GEOMETRY AND APPROXIMATIONS

Consider a geometry of a human body standing on the ground and being exposed to an electric field in the ELF-LF range, as shown in Fig. 22. The contacts between the feet, the hands, or other parts of the body and the ground are represented by the grounding impedances $Z_{L_i} (i=1-k)$. The shape and posture of the body can be realistic and arbitrary. The impressed electric field, which is maintained by a power line or other ELF or LF sources, is assumed to be spatially uniform over the body and oscillating with an angular frequency of ω . The time dependence factor of $\exp(j\omega t)$ will be assumed.

We aim to determine the surface-charge density and the electric field induced on the body's surface as well as the current density, the electric field, and the SAR induced inside the body. Also, we aim to determine the effects of the grounding impedance on the induced current. To simplify the problem, the following approximations, which have been proved valid [7], will be adopted.

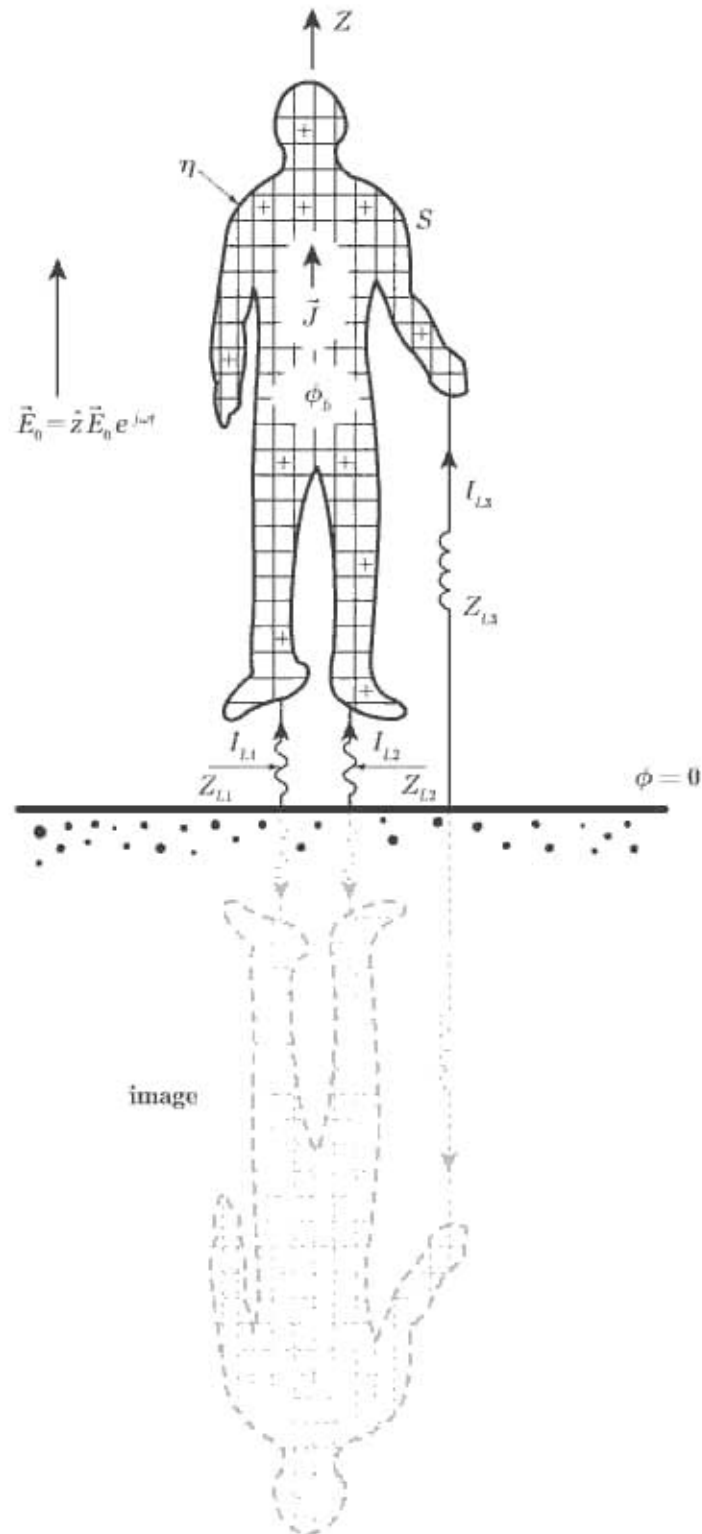


Fig. 22 A man standing on the ground is exposed to an electric field of ELF-LF range. The contacts between the feet and the left hand and the ground are represented by Z_{Li} ($i = 1 - 3$).

as the sum of the potential $\phi_s(\vec{r})$, which is maintained by the induced surface charge $\eta(\vec{r})$, and the potential $\phi_o(\vec{r})$, which is maintained by the impressed electric field. That is,

$$\phi_s(\vec{r}) + \phi_o(\vec{r}) = \phi_b \quad (4.10)$$

Using the quasi-static approximation and considering the ground image effect, $\phi_s(\vec{r})$ can be expressed as

$$\phi_s(\vec{r}) = \frac{1}{4\pi\epsilon_0} \int_{s, s_i} \eta(\vec{r}') \frac{1}{|\vec{r} - \vec{r}'|} ds' \quad (4.11)$$

where s is the body surface and s_i is the surface of the body image, \vec{r} is a field point on the body surface, and \vec{r}' represents a source point on the body surface and the image surface. The potential $\phi_o(\vec{r})$ can be expressed in terms of the impressed electric field. For the geometry of Fig. 22, $\phi_o(\vec{r}') = -E_0 z$. The body potential ϕ_b is an unknown quantity and its value depends on the body geometry, the impressed electric field, and the grounding impedances Z_{Lj} .

Equation (4.10) can be rewritten as

$$\frac{1}{4\pi\epsilon_0} \int_{s, s_i} \eta(\vec{r}') \frac{1}{|\vec{r} - \vec{r}'|} ds' + \phi_o(\vec{r}) = \phi_b \quad (4.12)$$

Equation (4.12) is an integral equation for the induced surface-charge density $\eta(\vec{r}')$, and with the body potential ϕ_b as another unknown.

To determine $\eta(\vec{r}')$ and ϕ_b , we need another equation. This second equation is obtained on the basis of Ohm's law and the conservation of electric charge. The total current flowing between the body and the ground is the sum of the currents flowing through the grounding impedances where Z_{Lj} :

$$I = \phi_b [1/Z_{L1} + 1/Z_{L2} + \dots + 1/Z_{Lk}] = \phi_b \sum_{i=1}^k 1/Z_{Li} \quad (4.13)$$

On the other hand, the total current I (flowing from the ground to the body) can be expressed in terms of the total surface charge, based on the conservation of electric charge, as

$$I = j\omega \int_S \eta(\vec{r}') ds' \quad (4.14)$$

Combining Eq. (4.13) and Eq. (4.14), we have

$$\phi_b = \frac{j\omega}{\sum_{l=1}^k 1/Z_{Ll}} \int_S \eta(\vec{r}') ds' \quad (4.15)$$

Eq. (4.15) is the desired second equation which has $\eta(\vec{r})$ and ϕ_b as the unknowns.

NUMERICAL SOLUTIONS—MOMENT METHOD

To solve Eq. (4.12) and Eq. (4.15) numerically for $\eta(\vec{r})$ and ϕ_b , the method of moments will be applied. The body surface S is partitioned into N subareas (patches) and the induced surface-charge density $\eta(\vec{r})$ on each subarea Δs_n ($n = 1 - N$) is assumed to be an unknown constant. Eq. (4.12) is then forced to be valid at the central points \vec{r}_n ($n = 1 - N$) of the N subareas. In other words, the method of moments approach is applied using pulse basis functions and delta testing functions (point matching). When Eq. (4.12) is point matched at the center of the m th subarea \vec{r}_m , it can be expressed as

$$\sum_{i=1}^k \frac{1}{4\pi\epsilon_0} \left[\int_{\Delta s_n} \frac{\eta_n ds'}{|\vec{r}_m - \vec{r}'|} - \int_{\Delta s_n} \frac{\eta_n ds'_i}{|\vec{r}_m - \vec{r}'_i|} \right] + \phi_b(\vec{r}_m) = \phi_b \quad (4.16)$$

where η_n is the surface-charge density at the n th subarea Δs_n and \vec{r}' is a source point within Δs_n .

The surface-charge density at the corresponding subarea ΔS_m of the body's image is $-\eta_n$ due to the image effect and \vec{r}' is a source point within ΔS_m . Equation (4.16) can be rewritten as

$$\sum_{n=1}^N M_{mn} \eta_n + \phi_0(\vec{r}_m) = \phi_b \quad (4.17)$$

where

$$M_{mn} = \frac{1}{4\pi\epsilon_0} \left[\int_{\Delta S_n} \frac{ds'}{|\vec{r}_m - \vec{r}'|} - \int_{\Delta S_{ni}} \frac{ds'_i}{|\vec{r}_m - \vec{r}'_i|} \right] \quad (4.18)$$

The integrals involved in Eq. (4.18) can be integrated numerically or analytically approximated when ΔS_n is small. It is noted that when $n=m$ for M_{mn} , \vec{r}_m is at the center of ΔS_m and \vec{r}' is within ΔS_m ; thus, $|\vec{r}_m - \vec{r}'|$ will vanish in the first integral of Eq. (4.18). However, this singularity is removable through the integration and it causes no difficulty.

Equation (4.17) can be used to generate N simultaneous equations when m is varied from 1 to N , that is, when Eq. (4.16) is point matched at the central points of the N subareas. This set of N simultaneous equations can be expressed in a matrix form as follows:

$$\begin{bmatrix} M_{11} & M_{12} & \cdots & M_{1N} & -1 \\ M_{21} & M_{22} & \cdots & M_{2N} & -1 \\ & & \cdots & & -1 \\ M_{N1} & M_{N2} & \cdots & M_{NN} & -1 \end{bmatrix} \begin{bmatrix} \eta_1 \\ \eta_2 \\ \vdots \\ \eta_N \\ \phi_b \end{bmatrix} = - \begin{bmatrix} \phi_{01} \\ \phi_{02} \\ \vdots \\ \phi_{0N} \end{bmatrix} \quad (4.19)$$

where $\phi_{0n} = \phi_0(\vec{r}_n)$. Notice that Eq. (4.19) represents a set of equations that is of $N \times (N+1)$ order. In order to solve $N+1$ unknowns ($\eta_1, \eta_2, \dots, \eta_N$ and ϕ_b), one more equation between η_n and ϕ_b is needed. This equation is provided by Eq. (4.15) as follows:

$$\sum_{n=1}^N \eta_n \Delta S_n = \frac{1}{j\omega} \left[\sum_{l=1}^k 1/Z_{ll} \right] \phi_b \quad (4.20)$$

When Eq. (4.20) is combined with Eq. (4.19), we have

$$\begin{pmatrix} M_{11} & M_{12} & \cdots & M_{1N} & -1 \\ M_{21} & M_{22} & \cdots & M_{2N} & -1 \\ & & & & -1 \\ M_{N1} & M_{N2} & \cdots & M_{NN} & -1 \\ \Delta S_1 & \Delta S_2 & & \Delta S_N & \frac{j}{\omega} \sum_{l=1}^k 1/Z_{Li} \end{pmatrix} \begin{pmatrix} \eta_1 \\ \eta_2 \\ \vdots \\ \eta_N \\ \phi_b \end{pmatrix} = - \begin{pmatrix} \phi_{01} \\ \phi_{02} \\ \vdots \\ \phi_{0N} \\ 0 \end{pmatrix} \quad (4.21)$$

Equation (4.21) represents an $(N+1) \times (N+1)$ matrix equation, and $(N+1)$ unknowns, $\{\eta_n\}$ and ϕ_b , can be easily determined by a matrix inversion or other appropriate methods.

There are two special cases of interest: 1) the case when the body is shorted to the ground, $Z_{Li} = 0$ for any i , and 2) the case when the body is isolated from the ground, $Z_{Li} = \infty$ for all i . For the short-circuit case, the body potential ϕ_b will be zero; therefore, Eq. (4.21) is reduced to an $N \times N$ matrix equation, with the last column and the last row of the matrix in Eq. (4.21) removed. The unknown surface-charge density $\{\eta_n\}$ can then be determined accordingly. For the isolated case, the last element of the matrix of Eq. (4.21), $\frac{j}{\omega} \sum_{l=1}^k \frac{1}{Z_{Li}}$ becomes zero. This implies that

$$\sum_{n=1}^N \eta_n \Delta S_n = 0 \quad (4.22)$$

that is, the total net charge on the body is zero. For this case, $\{\eta_n\}$ and ϕ_b are determined from Eq. (4.21) with the last element of the matrix set equal to zero.

After the induced surface-charge density η is determined, the induced electric field at the body surface is simply obtained from

$$E_s = \eta / \epsilon_0 \quad (4.23)$$

assuming that the induced electric field is totally perpendicular to the body surface.

The electric field enhancement factor is defined as the ratio of the induced electric field at the surface to the impressed electric field E_s/E_0 . This value can easily exceed 10 at the head or the tip of a stretched arm and hand. Thus, when a man is exposed to the electric field of an EHV power line, the induced electric field at some points of the body can be extremely large since E_0 is already a very high value in this case.

INDUCED CURRENT INSIDE THE BODY

After the induced surface-charge density at any point on the body surface is determined, the induced current density inside the body can be determined on the basis of the conservation of electric charge and Maxwell's equations.

The first quantity to be determined is the total sectional current at any cross section of the body. Referring to Fig. 23, we assume that the positive sectional current at any cross section of the body is directed towards the head. We will consider, for example, three sectional currents: the sectional current at the chest I_1 , the sectional current at the lower abdomen I_2 , and the sectional current at the right arm I_3 .

If we integrate the equation of the conservation of electric charge $\nabla \cdot \vec{J} + j\omega\rho = 0$ over the volume V_1 which includes the upper body above the chest cross section (see Fig. 23), we have

$$I_1 = - \int_{S_1} (\hat{n} \cdot \vec{J}_1) ds = j\omega \int_{S_1} \eta ds \quad (4.24)$$

where \hat{n} is the unit vector pointing outward from V_1 , S_{ct} is the cross-sectional area at position shown in Fig. 23, S_1 is the body surface above the chest cross section S_{ct} , and \vec{J}_1 is the current density at S_{ct} .

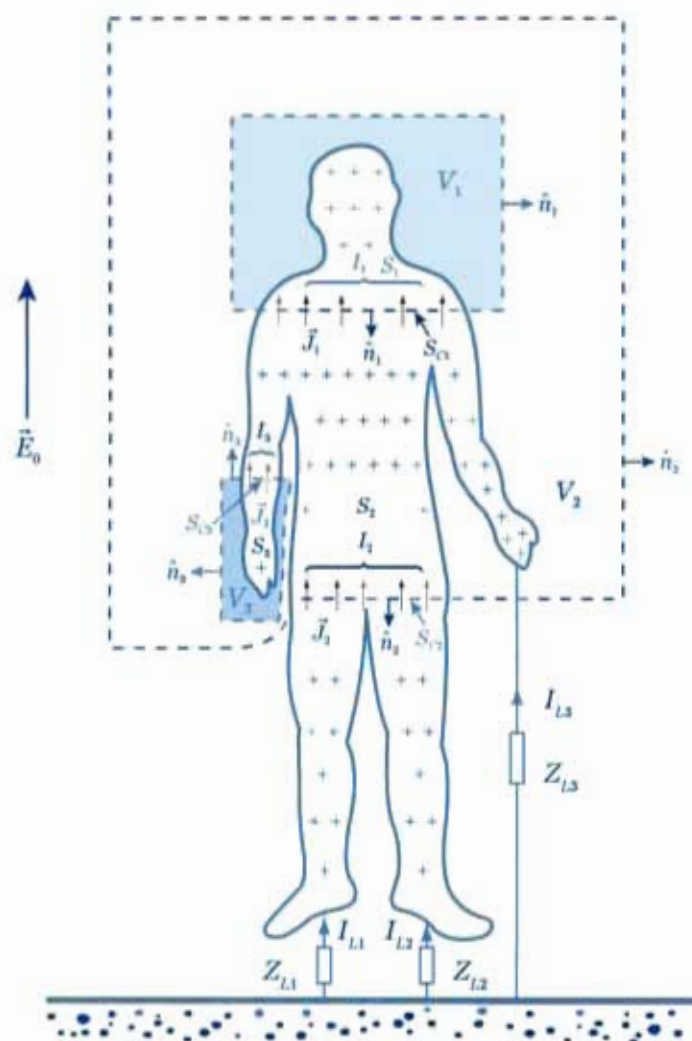


Fig. 23 Geometry for calculating the induced current in the body.

A similar integral over the volume V_2 , which includes the portion of the body above the lower abdomen and has a boundary surface cutting through the lower abdomen section S_2 and a grounding impedance Z_{L2} connecting the left hand to ground, will lead to

$$\int_{S_2} (\hat{n}_2 \cdot \vec{J}_2) ds - I_{L2} = -j\omega \int_{S_2} \eta ds$$

or

$$I_2 + I_{L2} = j\omega \int_{S_2} \eta ds \quad (4.25)$$

where \hat{n}_2 is the unit vector pointing outward from V_2 , \vec{J}_2 is the current density at S_{c2} , S_2 is the body surface enclosing by V_2 , and I_{L2} is the current flowing from the ground to the left hand through the grounding impedance Z_{L2} . I_{L2} is easily determined from ϕ_b/Z_{L2} .

Another similar integral over the volume V_3 which contains the right arm and hand leads to

$$I_3 = \int_{S_3} (\hat{n}_3 \cdot \vec{J}_3) ds = -j\omega \int_{S_3} \eta ds \quad (4.26)$$

where \hat{n}_3 is the unit vector pointing outward from V_3 , S_{c3} is the cross-sectional area as designated in Fig. 23, \vec{J}_3 is the current density at S_{c3} , and S_3 is the surface of the right arm and right hand enclosed by V_3 . It is noted that \hat{n}_3 and \vec{J}_3 are in the same direction; therefore, the expression of I_3 has a negative sign in Eq. (4.26). This negative sign will lead to the phenomenon that the current in the arm flows in the opposite direction to that flowing in other parts of the body.

One of the most important quantities concerning the body current is the short-circuit current I_{sc} , which is defined as the current flowing between the feet and the ground when the grounding impedances (Z_{L1} and Z_{L2}) between the feet and ground are zero. The other grounding impedances (e.g., Z_{L3}) between other parts of the body and ground are infinity (open circuit). I_{sc} can be easily obtained by the same approach as above, and is given by

$$I_{sc} = j\omega \int_S \eta ds \quad (4.27)$$

where S includes the total body surface and η is the induced surface-charge density at the body surface under the condition that the body's potential ϕ_b is zero.

After the determination of the sectional current, the volume density of the induced current inside the body \vec{J} can be determined from Maxwell's equation: $\nabla \times \vec{H} = (\sigma + j\omega\epsilon)\vec{E}$ or $\nabla \cdot [(\sigma + j\omega\epsilon)\vec{E}] = 0$. For the ELF-LF range, $\sigma \gg \omega\epsilon$ inside the body; therefore,

$$\nabla \cdot (\sigma \vec{E}) = \nabla \cdot \vec{J} \doteq 0 \quad (4.28)$$

Equation (4.28) can be used to predict the distribution of \vec{J} inside the body with the prior knowledge of the sectional current I at any cross section of the body.

Assume that \vec{J} at any cross section of the body has only two components: a longitudinal component \vec{J}_l and a radial component \vec{J}_r . This approximation assumes a cylindrical geometry for the body cross section and also ignores the circumferential component of \vec{J} .

The longitudinal component \vec{J}_l , can be approximately obtained as

$$\vec{J}_l = I / s_c \quad (4.29)$$

where I is the already determined total sectional current and s_c is the cross-sectional area of the body at the position where Eq. (4.29) is applied. The calculation of \vec{J}_l is valid for a homogeneous body, but it may also be a fair approximation for a heterogeneous body, based on the finding by Spiegel [13] using the electric field integral equation method that the induced current density \vec{J} is rather independent of the electric parameters of the body at the ELF range.

Now that \vec{J}_l is determined at any cross section of the body, the radial component \vec{J}_r can be derived from Eq. (4.28), using a cylindrical geometry, as follows.

From

$$\nabla \cdot \vec{J} = \frac{1}{r} \frac{\partial}{\partial r} (r J_r) + \frac{\partial}{\partial l} J_l = 0,$$

we have

$$\frac{\partial}{\partial r} (r J_r) = -r \left[\frac{\partial J_l}{\partial l} \right]$$

After integrating both sides, it gives

$$J_r = -\frac{r}{2} \left[\frac{\partial J_l}{\partial l} \right] \quad (4.30)$$

where r is the radial distance from the center of the cross section and $[\partial J_l / \partial l]$ is the rate of change of \vec{J}_l , in the longitudinal direction. Since \vec{J}_l is known at any cross section, the value of $[\partial J_l / \partial l]$ can be estimated easily. Equation (4.30) indicates that \vec{J}_r is zero at the center of the body and linearly increases toward the body surface. The direction of \vec{J}_r is dictated by the sign of $[\partial J_l / \partial l]$.

After \vec{J} is determined, the electric field induced inside the body is determined from

$$\vec{E} = \vec{J} / \sigma \quad (4.31)$$

and the SAR value is calculated via

$$\text{SAR} = \frac{1}{2\sigma} |\vec{J}|^2 / \rho \text{ W/kg} \quad (4.32)$$

where ρ is the volume density of mass in kg/m^3 .

NUMERICAL RESULTS AND COMPARISON TO EXPERIMENTS

We have generated many useful numerical results on the induced electric fields at the body surface and inside the body, the induced current, the SAR, and effects of the grounding impedance on the short-circuit current. Since these results are quite extensive, only a few numerical results will be compared to the experimental results to validate the accuracy of the present method.

The first check of our method was made by comparing the numerical results of the induced electric field on an isolated conducting sphere to its exact solution. The agreement was found to be within 1 percent. We then verified the accuracy of our method by comparing the numerical

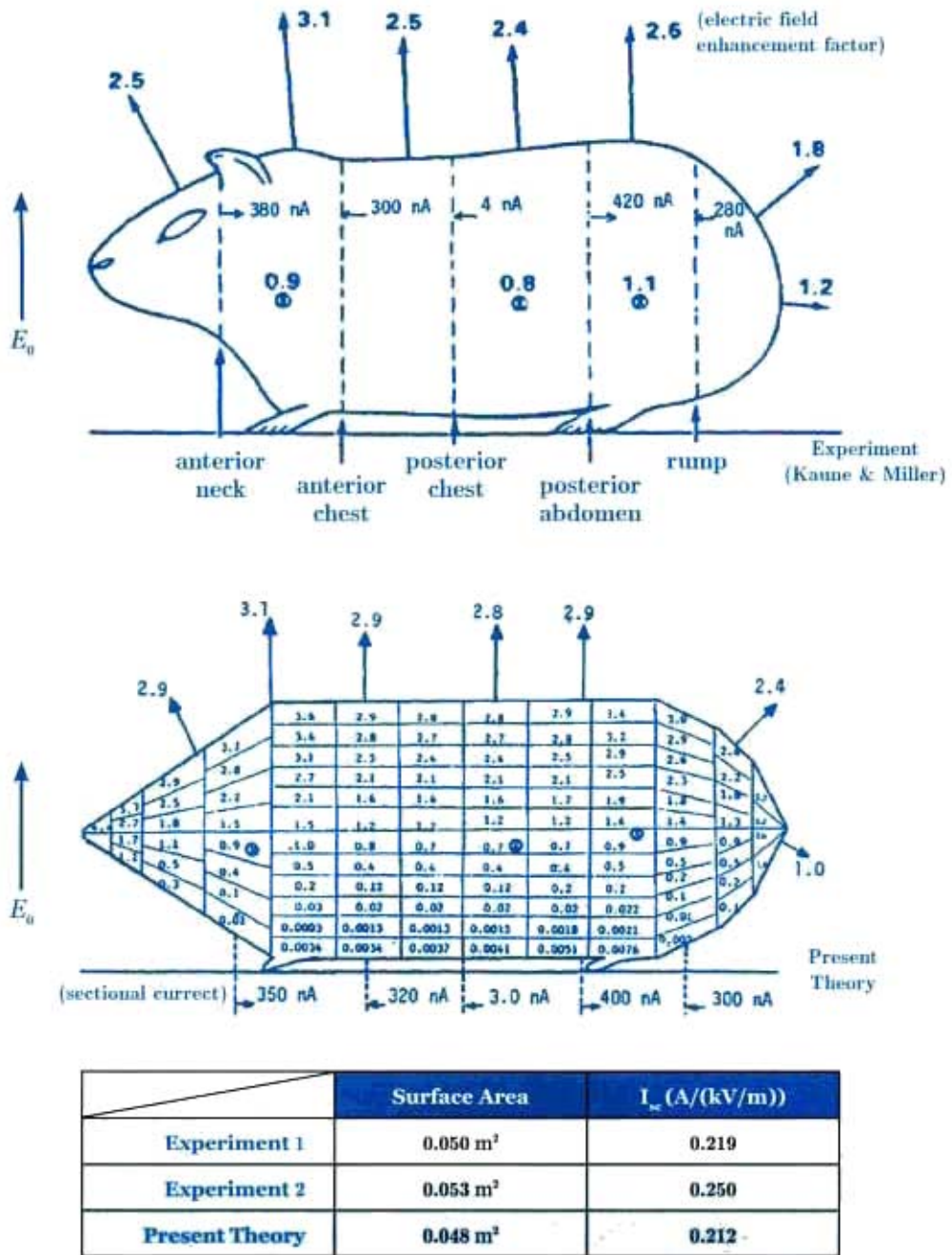


Fig. 24 Comparison of theoretical results by present method to experimental results of Kaune and Miller on electric field enhancement factor, sectional current, and short-circuit currents for grounded guinea pig exposed to 10 kV/m, 60 Hz electric field.

results on the electric field enhancement factor, the sectional current, and the short-circuit current induced by a 60 Hz electric field of 10 kV/m in a theoretical model of a guinea pig which simulated the actual animal used by Kaune and Miller [9] to their experimental results. Fig. 24 shows the comparison between the experimental and numerical results. The upper part of Fig. 24 shows the electric field enhancement factors measured at various locations on the surface and the sectional currents at five cross sections of a guinea pig. The lower part shows the electric field enhancement factors at various points and five sectional currents calculated for the theoretical model of the guinea pig. Good agreement is obvious when the corresponding experimental and numerical values of these quantities shown in these two figures are compared. The table at the bottom of Fig. 24 indicates the comparison of the measured short-circuit current and the calculated values. The measured short-circuit currents for two guinea pigs were 0.219 and 0.225 $\mu\text{A}/(\text{kV}/\text{m})$ and our calculated result was 0.212 $\mu\text{A}/(\text{kV}/\text{m})$. The results shown in Fig. 24 demonstrate the accuracy of our method. It is noted that in the numerical calculation, the body surface of the guinea pig was partitioned into 228 patches. This leads to 114 unknowns when a half-body symmetry was applied.

Our method was also employed to compute the current density induced by a 60 Hz electric field of 10 kV/m in a phantom model of man, 45 cm in height, used by Kaune and Forsythe [10]. Fig. 25 depicts the comparison of the experimental and numerical results of the induced current density. In the numerical calculation, the body surface was partitioned into 472 patches, leading to 118 unknowns with a quarter-body symmetry. The right figure shows the measured current densities at various points inside the body. The induced current density is mainly longitudinal (or vertical) with a small radial (or horizontal) component as shown.

Notice that the direction of the radial component is outward in the chest region, but is inward at the neck and the abdominal region. The most interesting observation is that the induced current in the arm is directed downward or in the opposite direction to that flowing in other parts of the body. The numerical results for the induced current density in the theoretical

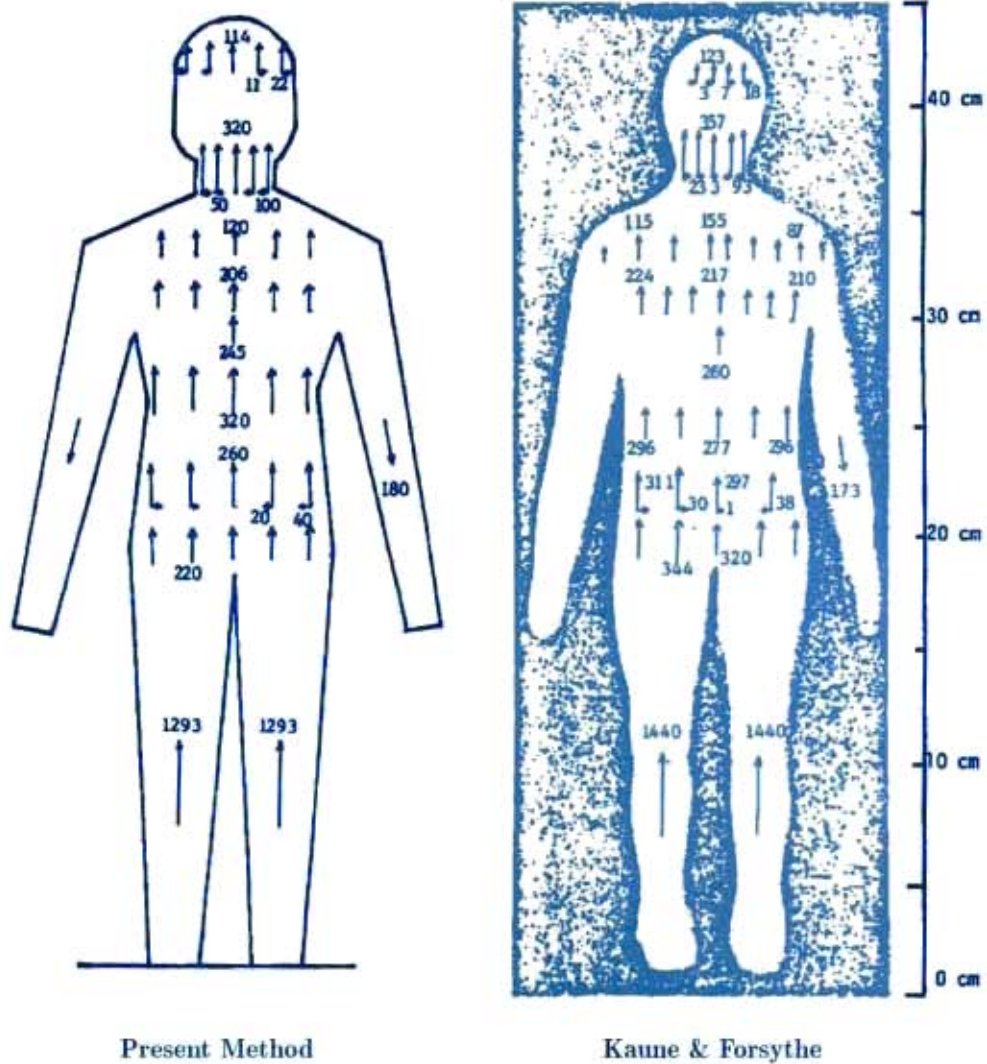


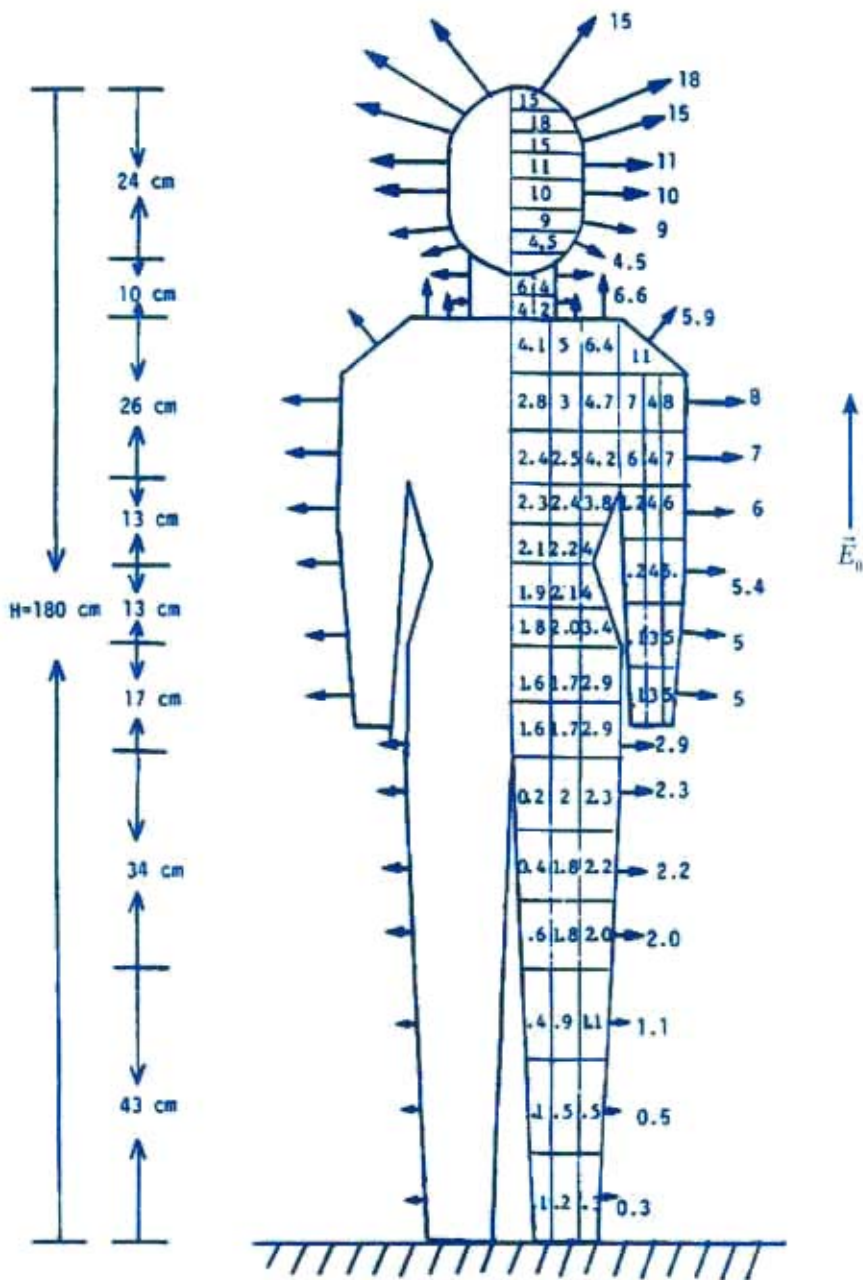
Fig. 25 Comparison of theoretical results by the present method to experimental results of Kaune and Forsythe on vertical and horizontal current densities for a grounded human model exposed to 10 kV/m, 60 Hz electric field. Induced current densities are given in units of nA/cm².

model which approximates the experimental model are shown in the left figure. The computed current densities, in amplitude and direction, at various locations inside the body agree very well with the measured values.

The agreement between experiment and theory is within 5-10 percent on the amplitude. It is noted that the theory correctly predicted the reversed direction of the induced current in the arm and the directions of the radial components of the currents at different parts of the body. The results of Fig. 25 give a positive verification of the accuracy of our method.

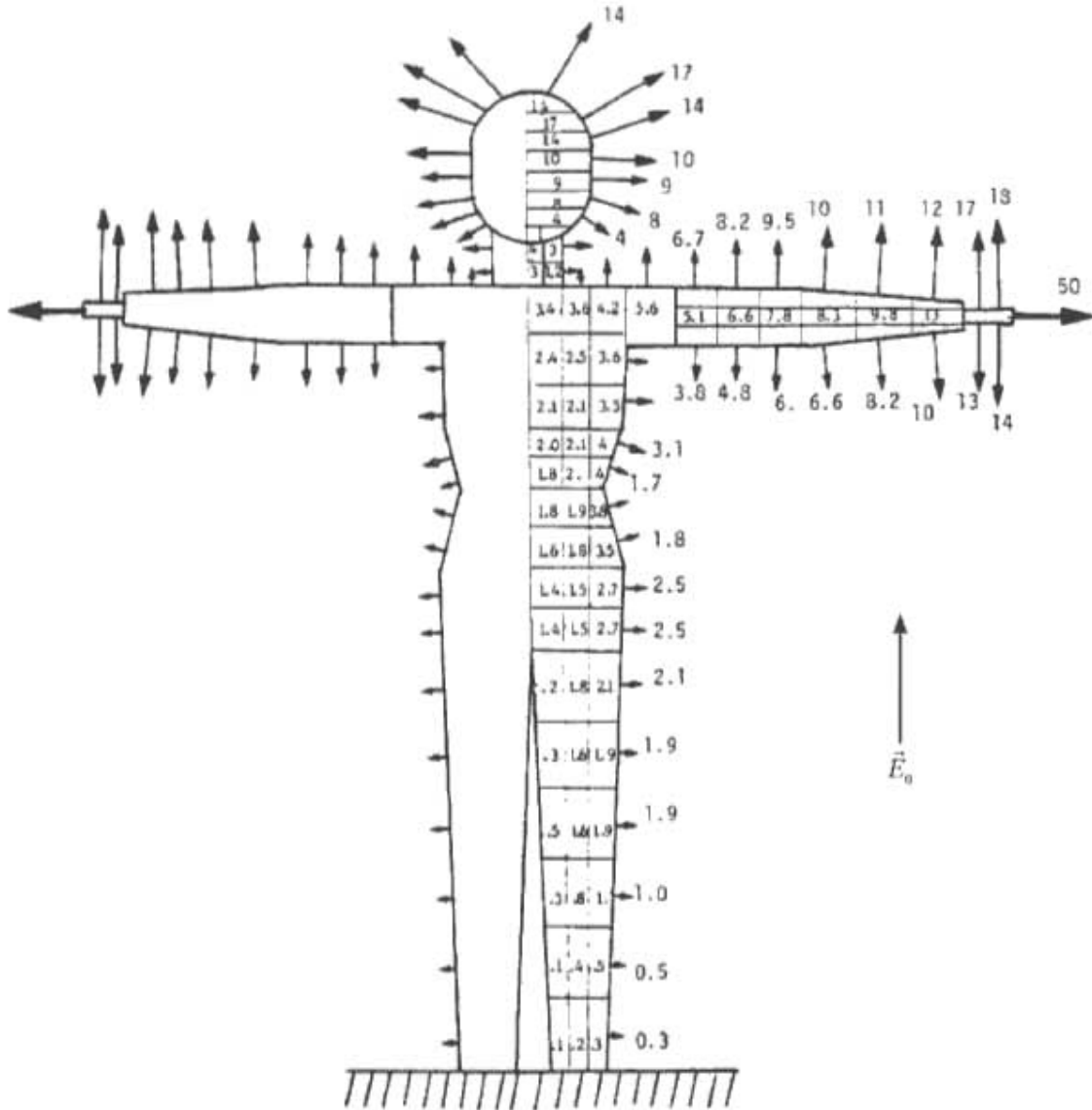
It is appropriate to give a few more selected numerical results on the interaction of a 60 Hz electric field with a human body. Fig. 26 depicts the calculated electric field enhancement factors at the surface of a man with a height of 180 cm and a weight of 68.2 kg standing upright and in direct contact (short-circuited case) with the ground, and who is exposed to a 60 Hz electric field of 1 kV/m. The enhancement factor can vary from 0.1 to about 20 over the body surface. Also shown in Fig. 26 is the calculated short-circuit current of 18.0 μA . This value is very close to 17.5 μA , which is calculated with an empirical formula of $I_{sc} = 5.4 \cdot 10^{-9} \cdot H^2 \cdot E \cdot f / 60$ used by Chiba et al. [14]. In the numerical calculation, the body's surface was partitioned into 424 patches leading to 106 unknowns with a quarter-body symmetry.

Fig. 27 shows the calculated electric field enhancement factors and the short-circuit current in the same man with stretched arms induced by the same electric field as the case of Fig. 26. It is observed that the electric field enhancement factor can be very high at the tip of the hand due to its sharp geometry. Also, it is noted that when the arms are stretched, the short-circuit current is increased to 23.3 μA as predicted by our method. This value is quite different from the value of 17.5 μA if the same formula used by Chiba et al. [14] is used. This indicates the phenomenon that the induced electric field at the body surface and the short-circuit current, and consequently the induced current inside the body, are strongly dependent on the body geometry and position. Even though the phenomena involved are rather complicated, this method is capable of predicting them.



$I_{sc} = 18.0 \mu\text{A}$ (Present theory)
 $I_{sc} = 17.5 \mu\text{A}$ (Based On $I_{sc} = 5.4 \cdot 10^{-9} \cdot H^2 \cdot E \cdot f/60$ see Chiba et al.)

Fig. 26 Theoretical results on electric field enhancement factors and short-circuit current for a realistic model of man standing on the ground being exposed to 1kV/m, 60 Hz electric field.



$$I_{sc} = 23.3 \mu\text{A} \text{ (Present theory)}$$

$$I_{sc} = 17.5 \mu\text{A} \text{ (Based On } I_{sc} = 5.4 \cdot 10^{-9} \cdot H^2 \cdot E \cdot t / 60)$$

Fig. 27 Theoretical results on electric field enhancement factors and short-circuit current for a realistic model of man with hands stretching horizontally and standing on the ground plane being exposed to 1 kV/m, 60 Hz electric field.

One more bit of interesting information on the effects of the grounding impedance on the short-circuit current of a man exposed to 60 Hz electric field of 1 kV/m is given in Fig. 28. The grounding impedance is assumed to be resistive, capacitive, or inductive. The short-circuit current is found to remain practically unchanged, maintaining a value of about 18 $\mu\text{A}/(\text{kV}/\text{m})$ when the grounding impedance is varied from 0 to 10 $\text{M}\Omega$. Only after the grounding impedance exceeds the value of 10 $\text{M}\Omega$ does the short-circuit current start to fall for a resistive or a capacitive grounding impedance. For an inductive grounding impedance, there is a possible resonance

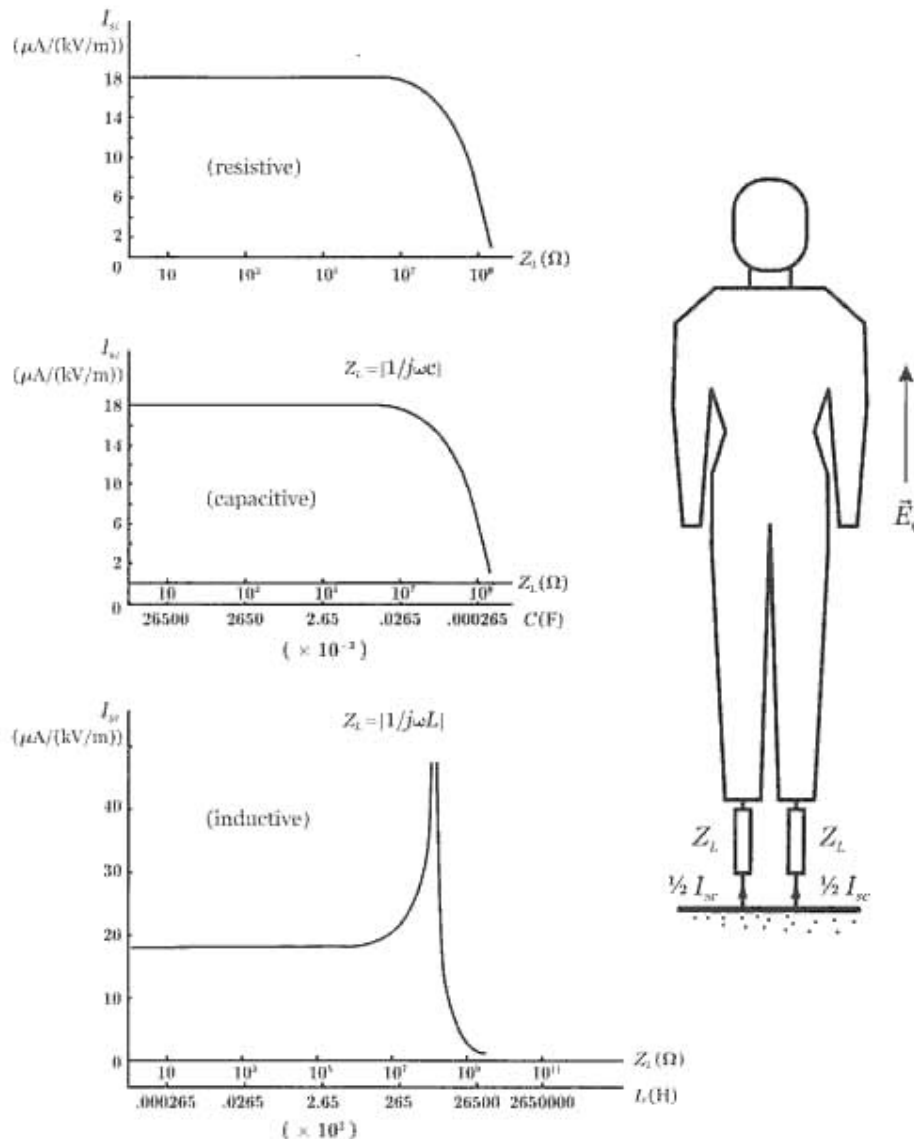


Fig. 28 Short-circuit current as a function of grounding impedance.

phenomenon when the impedance has a value on the order of $100 \text{ M}\Omega$, corresponding to an inductance of $3 \times 10^5 \text{ H}$. This implies that in a very unlikely case when the grounding impedance is an extremely large inductance of about $3 \times 10^5 \text{ H}$, there may be a very large current induced in the body.

The numerical examples given so far are all computed for the case of 60 Hz. However, our method has also been employed to predict the short-circuit currents induced by HF electric fields in a human body. Table I shows a comparison of experimental results on the short-circuited current, measured by various workers [17] at frequencies between 60 Hz and 27 MHz, and the corresponding numerical results generated by our method. A satisfactory agreement was obtained between theory and experiment up to about 30 MHz. This indicates that our method may be applicable up to the HF range or at least up to the LF range.

Table I

Comparison of experimental and empirical results on short-circuit current and theoretical results by present method

f_{MHz}	I_{sc} in (mA/(V/m))		
	$h_m = 1.75 \text{ m}$ Eq.(+)	$h_m = 1.75 \text{ m}$ Measured	$h_m = 1.80 \text{ m}$ Present Theory (SCIE)
Subjects Barefoot			
0.63	0.208	0.210	0.189
0.70	0.232	0.280	0.212
1.51	0.499	0.391	0.453
27.405	9.060	9.330	8.230
Subjects Barefoot, Both Arms Raised			
0.70		0.384	0.272
1.51		0.555	0.586
27.405		9.85	10.60
Comparison Data			
0.72 [13]	0.238	0.277	0.216
0.92	0.304	0.316	0.276
1.145	0.379	0.366	0.344
1.35	0.447	0.405	0.405
1.47	0.486	0.56	0.441
0.146 [14]	0.048	0.035	0.044
27.0 [15]	8.93	8.4	8.13

* $I_{\text{sc}} = 0.108 \cdot h_m^2 \cdot E_0 \cdot f_{\text{MHz}} [\text{mA}/(\text{V}/\text{m})]$.

REFERENCES

- [1] Chen, K.M., Misra, D., Wang, H., Chuang, H.R. and Postow, E., "An X-band Microwave Life-Detection System," *IEEE Trans. On Biomedical Engineering*, Vol. 33, pp. 697-701, 1986.
- [2] Chen, Kun-Mu, "Active remote physiological monitoring using Microwaves," *Medical monitoring in the home and work environment*, Edited by Laughton E. Miles and Roger J. Broughton, Raven Press, New York (1990).
- [3] Harrington, R.F. (1961), *Time Harmonic Electromagnetic Fields*, McGraw-Hill Book Co., New York.
- [4] Chen Kun-Mu, Yong Huang, Jianping Zhang, and Adam Norman, "Microwave life-detection systems for searching human subjects under earthquake rubble or behind barrier," *IEEE Trans. on Biomedical Engineering*, Vol. 27, No.1, pp. 105-114, Jan. 2000.
- [5] D. W. Deno, "Currents induced in the human body by high voltage transmission line electric field-Measurement and calculation of distribution and dose," *IEEE Trans. Power App. Syst.*, vol. PAS-96, pp. 1517-1527, Sept./Oct. 1977.
- [6] A. W. Guy, M. D. Webb, and C. C. Sorensen, "Determination of power absorption in man exposed to high frequency electromagnetic fields by thermographic measurements on scale models," *IEEE Trans. Biomed. Eng.*, vol. BME-23, pp. 361-371, 1976.
- [7] W. T. Kaune and M. F. Gillis, "General properties of the interaction between animals and ELF electric fields," *Bioelectromagn.*, vol. 2, pp. 1-11, 1980.
- [8] W. T. Kaune and R. D. Phillips, "Comparison of the coupling of grounded humans, swine and rats to vertical, 60-Hz electric fields," *Bioelectromagn.*, vol. 1, pp. 117-129, 1980.
- [9] W. T. Kaune and M. C. Miller, "Short-circuit currents, surface electric fields, and axial current densities for guinea pigs exposed to ELF electric fields," *Bioelectromagn.*, vol. 5, pp. 361-364, 1984.
- [10] W. T. Kaune and W. C. Forsythe, "Current densities measured in human models exposed to 60 Hz electric fields," *Bioelectromagn.*, vol. 6, pp. 13-32, 1985.

- [11] Y. Shiau and A. R. Valentino, "ELF electric field coupling to dielectric spheroidal models of biological objects," *IEEE Trans. Biomed. Eng.*, vol. BME-28, pp. 429-437, June 1981.
- [12] R. J. Spiegel, "High-voltage electric field coupling to humans using moment method techniques," *IEEE Trans. Biomed. Eng.*, vol. BME- 24, pp. 466-472, Sept. 1977.
- [13] —, "Numerical determination of induced currents in humans and baboons exposed to 60-Hz electric fields," *IEEE Trans. Electromagn. Compat.*, vol. EMC-23, pp. 382-390, Nov. 1981.
- [14] A. Chiba, K. Isaka, and M. Kitagawa, "Application of finite element method to analysis of induced current densities inside human model exposed to 60-Hz electric field," *IEEE Trans. Power App. Syst.*, vol. PAS-103, pp. 1895-1902, July 1984.
- [15] W. T. Kuane and F. A. McCreary, "Numerical calculation and measurement of 60-Hz current densities induced in an upright grounded cylinder," *Bioelectromagn.*, vol. 6, pp. 209-220, 1985.
- [16] Kun-Mu Chen, Huey-Ru Chuang and Chun-Ju Lin, "Quantification of interaction between ELF-LF electric fields and human bodies," *IEEE Trans. Biomed. Eng.*, vol. BME-33, No.8, pp 746-756, Aug. 1986.
- [17] O. P. Gandhi, I. Chatterjee, D. Wu, and Y. G. Gu, "Likelihood of high rates of energy deposition in the human legs at ANSI recommended 3-30 MHz RF safety levels," *Proc. IEEE*, vol. 73, pp. 1145- 1147, June 1985.